ANTIOXIDANTS & REDOX SIGNALING
Volume 32, Number 6, 2020

DOI: 10.1089/ars.2018.7690

Discoveries

FORUM ORIGINAL RESEARCH COMMUNICATION

Structural and Functional Characterization of the Globin-Coupled Sensors of *Azotobacter vinelandii* and *Bordetella pertussis*

Francesca Germani,[1] Marco Nardini,[2] Amy De Schutter,[3] Bert Cuypers,[3] Herald Berghmans,[1] Marie-Louise Van Hauwaert,[1] Stefano Bruno,[4] Andrea Mozzarelli,[4] Luc Moens,[1] Sabine Van Doorslaer,[3] Martino Bolognesi,[2] Alessandra Pesce,[5] and Sylvia Dewilde[1]

Abstract

Aims: Structural and functional characterization of the globin-coupled sensors (GCSs) from *Azotobacter vinelandii* (*Av*GReg) and *Bordetella pertussis* (*Bpe*GReg).
Results: Ultraviolet/visible and resonance Raman spectroscopies confirm the presence in *Av*GReg and *Bpe*-GReg of a globin domain capable of reversible gaseous ligand binding. In *Av*GReg, an influence of the transmitter domain on the heme proximal region of the globin domain can be seen, and k'_{CO} is higher than for other GCSs. The O_2 binding kinetics suggests the presence of an open and a closed conformation. As for *Bpe*GReg, the fully oxygenated *Av*GReg show a very high diguanylate cyclase activity. The carbon monoxide rebinding to *Bpe*GReg indicates that intra- and intermolecular interactions influence the ligand binding. The globin domains of both proteins (*Av*GReg globin domain and *Bpe*GRegGb with cysteines (Cys16, 45, 114, 154) mutated to serines [*Bpe*GReg-Gb*]) share the same GCS fold, a similar proximal but a different distal side structure. They homodimerize through a G-H helical bundle as in other GCSs. However, *Bpe*GReg-Gb* shows also a second dimerization mode.
Innovation: This article extends our knowledge on the GCS proteins and contributes to a better understanding of the GCSs role in the formation of bacterial biofilms.
Conclusions: *Av*GReg and *Bpe*GReg conform to the GCS family, share a similar overall structure, but they have different properties in terms of the ligand binding. In particular, *Av*GReg shows an open and a closed conformation that in the latter form will very tightly bind oxygen. *Bpe*GReg has only one closed conformation. In both proteins, it is the fully oxygenated GCS form that catalyzes the production of the second messenger. *Antioxid. Redox Signal.* 32, 378–395.

Keywords: heme-based sensor, oxygen affinity, c-di-GMP and enzyme specificity, biofilm, crystal structure

Introduction

GLOBIN-COUPLED SENSORS (GCSs) are heme-based molecules widespread in bacteria and Archaea, consisting of chimeric proteins characterized by an N-terminal globin sensor domain coupled to a variety of C-terminal transmitter domains. Classification based on the function of the latter distinguishes: diguanylate cyclase (DGC), phosphodiesterase (PDE), histidine kinase, methyl-accepting chemotaxis, and a transmembrane function (20, 33).

[1]Department of Biomedical Sciences, University of Antwerp, Wilrijk, Belgium.
[2]Department of Biosciences, University of Milano, Milano, Italy.
[3]Department of Physics, University of Antwerp, Wilrijk, Belgium.
[4]Department of Food and Drugs, University of Parma, Parma, Italy.
[5]Department of Physics, University of Genova, Genova, Italy.

Innovation

Biofilms are considered an important medical and industrial issue and, consequently, globin-coupled sensors (GCSs) with diguanylate cyclase activity are becoming a class of enzymes of increasing scientific interest. This article extends the knowledge on the GCS proteins. It provides a comprehensive biochemical and structural characterization of *Azotobacter vinelandii* and *Bordetella pertussis* O_2 sensors involved in the control of biofilm formation and biofilm maintenance through the production of the cyclic-di-(3′,5′)-GMP second messenger.

The globin domain exhibits an efficient sensor function based on the reactivity of the heme iron atom (56, 69). Its structure is a variant of the 3-over-3 helical fold with an extra N-terminal Z-helix and no D-helix (45, 63, 70, 75). Binding of diatomic gaseous ligands causes a conformational change of the sensor domain that is transferred *via* a linker region to the transmitter domain, regulating its activity. A comprehensive model for a full-length GCS has been proposed for *Escherichia coli* globin-coupled sensor with DGC activity (*Ec*DosC) (63), although the precise mechanism of signal transduction within the molecule has still to be elucidated further.

Most known GCSs have a transmitter domain mainly consisting of a GGDEF domain with the DGC activity. GCSs with the DGC (or PDE) activity produce (or degrade) cyclic-di-(3′,5′)-GMP (c-di-GMP), a key second messenger involved in the conversion from a free-living into a sessile-living bacterial population through biofilm formation (23, 32, 57) and modulation of pathogenic factors (53). Bacteria in a biofilm show resistance to antibiotics and the host immune system and often result in persistent and chronic diseases (16). As such, biofilms are considered an important medical and industrial issue, and consequently, GCSs with the DGC activity are becoming of increasing scientific interest. Two examples of such biofilm-forming bacteria with a GCS are *Azotobacter vinelandii* and *Bordetella pertussis*.

A. vinelandii is a gram-negative, alginate-biofilm-producing bacterium, capable of diazotrophic growth and N-fixation in the presence of O_2 (48). As such, it has economic importance and it is widely used as a research model system. Genomic analysis revealed the presence of a GCS (globin-coupled sensor from *A. vinelandii* [*Av*GReg]) (55, 64). *Av*GReg is a 472 residues soluble protein consisting of a 178 residues N-terminal *Av*Greg globin sensor domain (*Av*GReg-Gb) and a 170 residues C-terminal GGDEF transmitter domain endowed with the DGC activity.

B. pertussis is a gram-negative, aerobic, biofilm-forming bacterial pathogen (9, 36, 73). It is the causative of pertussis or whooping cough, a highly contagious human disease that still causes, yearly, many deaths among children worldwide. In the *B. pertussis* genome, one GCS with gene-regulating function has been identified, namely globin-coupled sensor from *B. pertussis* (*Bpe*GReg) (3, 4).

As *Av*GReg, *Bpe*GReg is a di-domain molecule (475 residues) consisting of a globin-like sensor domain (residues: 1–155) covalently attached by a linker region (residues: 156–296) to a transmitter domain (residues: 297–475) with the DGC activity. This enzymatic activity is regulated by ligand (O_2) binding to the sensor domain, product (c-di-GMP) binding to an inhibitory site (RxxD motive in the transmitter domain), and the oligomerization state (mono-, di-, or tetramer) of the full GCS protein (6, 7, 50, 70). The participation of c-di-GMP in the process of biofilm formation of *Bpe*GReg has been demonstrated *in vivo* (70). The iron-bound O_2 is stabilized by a TyrB10 and SerE11 residue of the globin sensor domain. Dimerization of this domain involves the G and H helices (7, 50).

*Av*GReg and *Bpe*GReg not only merit scientific attention due to their respective economic and medical importance, but a thorough comparison of the structural and functional properties of these two molecules can contribute to a better understanding of the general role of GCSs in the signaling mechanism associated with the formation of bacterial biofilms.

We have therefore combined different biochemical and biophysical techniques to unravel the structural–functional relationship of these two proteins. The study involves the comparative analysis of the *Av*GReg and *Bpe*GReg full-length molecules, their respective globin domains, and some mutants (*Av*Greg with Tyr(44) mutated to Phe [*Av*GRegYB10F]) and Cys-mutant *Bpe*Reg*). In the latter notation, asterisk indicates the Cys-Ser mutation of Cys16, Cys45, Cys114, and Cys154, needed for crystallization purposes (see the Materials and Methods section for details). Moreover, the full-length *Av*GReg was for the first time obtained *via in vivo* folding, which led to a molecule with marked differences in the ligand binding properties than reported earlier for *in vitro*-folded *Av*GReg (from now on referred to as †*Av*GReg) (64).

Results

Ultraviolet/visible spectroscopy

The absorbance maxima of the ultraviolet/visible (UV/Vis) spectra of the full-length *Av*GReg and *Bpe*GReg in different ligation forms are reported in Table 1. The spectra of the ''as purified'' forms are typical for low-spin O_2-ligated ferrous globins, whereas those of the reduced forms are characteristic for ferrous high-spin pentacoordination of the heme. The absorbance maxima do not change for the truncated proteins consisting only of the globin domains (*Av*GReg-Gb and *Bpe*GReg-Gb) nor for the Cys mutant (*Bpe*GReg with cysteines (Cys16, 45, 114, 154) mutated to serines [*Bpe*GReg*]) and the YB10F mutant of *Av*GReg (data not shown). Overall, these results confirm the presence of a globin domain capable of gaseous ligand binding, and they are comparable to what was already reported for GCS in the literature (50, 70).

Resonance Raman spectroscopy

The resonance Raman (RR) spectra for *Av*GReg(-Gb) and *Bpe*GReg(-Gb) were recorded in the as-purified (O_2-bound ferrous) state and in the dithionite-reduced (deoxy ferrous) state (Fig. 1). The corresponding spectra of *Bpe*GReg* and *Bpe*GReg-Gb* [*Bpe*GRegGb with cysteines (Cys16, 45, 114, 154) mutated to serines] are depicted in Supplementary Figure S1. The high-frequency region (1300–1800 cm^{-1}) of the spectrum provides insights on the oxidation (ν_4), coordination (ν_3), and spin (ν_2) states of the heme iron atom (59) (Fig. 1B, D and Table 2).

The observed marker frequencies are in accordance with those reported for sperm whale myoglobin (*Sw*Mb) (60, 61) and different gas sensor proteins, such as the *Bacillus subtilis* heme-

Table 1. Ultraviolet/Visible Maxima of the Different Forms of Globin-Coupled Sensor from *Azotobacter vinelandii* and Globin-Coupled Sensor from *Bordetella pertussis*

*Av*GReg (wavelength in nm)					
As purified (Fe^{2+}-O_2)	413		541		580
Reduced (Fe^{2+})		434		560	
CO-ligated		421	542	568	
*Bpe*GReg (wavelength in nm)					
As purified (Fe^{2+}-O_2)	415		547		582
Reduced (Fe^{2+})		432		561	
CO-ligated		422	544	570	

*Av*GReg, globin-coupled sensor from *A. vinelandii*; *Bpe*GReg, globin-coupled sensor from *B. pertussis*; CO, carbon monoxide.

based aerotaxis transducer (*Bs*HemAT) (2), the isolated globin domain of *Ec*DosC (*Ec*DosC-heme) (28), and the globin-coupled histidine kinase from *Anaeromyxobacter* sp. Fw109-5 (*Af*GcHK) (29) (Table 2). They confirm the assignment of the ferrous form of *Av*GReg(-Gb) and *Bpe*GReg to a high-spin pentacoordinated heme site.

The as-purified proteins are all in the O_2-ligated ferrous form. Interestingly, the RR spectrum of *Bpe*GReg (Fig. 1D.a) reveals partial photolysis of the O_2 ligand (two ν_4 bands at 1359 and 1373 cm^{-1}, agreeing with the deoxy and oxy ferrous form). The partial photolysis hampers the analysis of the low-frequency part of the RR spectra of O_2-*Bpe*GReg, which will therefore not be considered in the below discussion.

The low-frequency region (200–900 cm^{-1}) reveals in-plane and out-of-plane vibrational modes of the heme (59). The $\nu_{Fe\text{-}His}$ is observed at 227 cm^{-1} for the ferrous-unligated *Av*GReg (Fig. 1A.b). This value is similar to that of ferrous *Bs*HemAT (225 cm^{-1}) (2) and *Ec*DosC-heme (227 cm^{-1}) (28). The $\nu_{Fe\text{-}His}$ peak broadens and shifts to ~214 cm^{-1} for *Av*GReg-Gb (Fig. 1A.d). For all deoxy ferrous *Bpe*GReg* and *Bpe*GReg-Gb* forms, the $\nu_{Fe\text{-}His}$ mode is observed as a broad peak around 229–233 cm^{-1} (Fig. 1C.b, C.d and Supplementary Fig. S1A.b, A.d).

The $\nu_{Fe\text{-}His}$ stretching mode is known to depend on different parameters (2, 39, 43). The higher $\nu_{Fe\text{-}His}$ mode found in ferrous-unligated *Av*GReg and *Bpe*GReg can indicate a stronger H-bonding to the proximal His N^{δ} nitrogen, less strain on the Fe-His bond, and/or a smaller dihedral angle φ between imidazole plane and the nearest N(pyrrole)-Fe-N(pyrrole) axis. Thus, in keeping with the sensor functionality, the $\nu_{Fe\text{-}His}$ difference observed between *Av*GReg and *Av*GReg-Gb points to an influence of the signaling domain on the heme proximal region of the globin domain.

Similarly, the γ_7 pyrrole bending mode, observed usually between 288 and 313 cm^{-1} in heme proteins and indicative of an out-of-plane distortion of the heme, changes slightly from a sharp peak at 301 cm^{-1} for deoxy *Av*GReg to a broadened peak at 299 cm^{-1} for deoxy ferrous *Av*GReg-Gb (Fig. 1A).

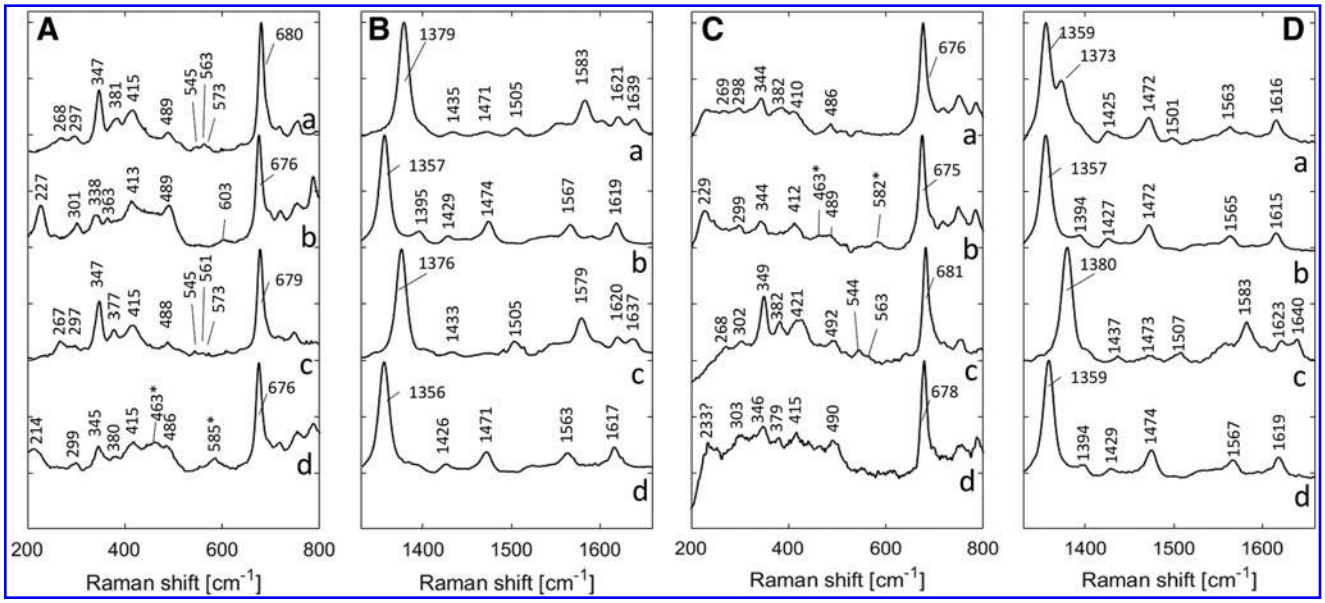

FIG. 1. RR spectra of *Av*GReg. RR spectra of *Av*GReg **(A.a, A.b, B.a, B.b)** and *Av*GReg-Gb **(A.c, A.d, B.c, B.d)** in the low-frequency region **(A)** and high-frequency region **(B)** and RR spectra of *Bpe*GReg **(C.a, C.b, D.a, D.b)** and *Bpe*GReg-Gb **(C.c, C.d, D.c, D.d)** in the low-frequency region **(C)** and high-frequency region **(D)**. Traces **(A–D.a, A–D.c)** show the RR spectra of the proteins as purified [oxygenated Fe(II) state], traces **(A–D.b, A–D.d)** show the RR spectra of the dithionite-reduced proteins (ferrous state). Wavenumbers marked with *asterisk* indicate reminiscent contributions of dithionite as described in Ref. (8). *Av*GReg, globin-coupled sensor from *Azotobacter vinelandii*; *Av*GReg-Gb, *Av*GReg globin domain; *Bpe*GReg, globin-coupled sensor from *Bordetella pertussis*; *Bpe*GReg-Gb, *Bpe*GReg globin domain; RR, resonance Raman.

Table 2. Resonance Raman Vibrational Modes Values of Different Hemoproteins

Hemoprotein	*Vibrational modes (cm^{-1})*					*References*
	ν_4	ν_3	ν_2	$\nu_{Fe\text{-}His}$	$\nu_{Fe\text{-}O2}$	
O_2-*Av*GReg	1379	1505	1583	—	563/573	This study
*Av*GReg (FeII)	1357	1474	1567	227	—	
O_2-*Av*GReg-Gb	1376	1505	1579	—	561/573	
*Av*GReg-Gb (FeII)	1356	1471	1563	214(b)	—	
O_2-*Bpe*GReg	1373	1501	n.d.	—	n.d.	This study
*Bpe*GReg (FeII)	1357	1472	1565	229	—	
O_2-*Bpe*GReg-Gb	1380	1507	1583	—	563	
*Bpe*GReg-Gb (FeII)	1359	1474	1567	233	—	
O_2-*Bpe*GReg*	1373	1502	1577	—	556	This study
*Bpe*GReg* (FeII)	1356	1472	1564	229	—	
O_2-*Bpe*GReg-Gb*	1375	1502	1578	—	560	
*Bpe*GReg-Gb* (FeII)	1356	1472	1564	230(b)	—	
O_2-*Sw*Mb	1377	1507	1584	—	569	(60, 61)
*Sw*Mb (FeII)	1356	1473	1564	220	—	
†*Av*GReg (FeIII)	1375	1506	1588	—	—	(64)
†*Av*GReg (FeII)	1361	1470	1592	n.d.	—	
†O_2-*Av*GReg178	1372	1502	1575	—	n.d.	
†*Av*GReg178 (FeII)	1354	1470	1562	220	—	
O_2-*Bs*HemAT	1372	1501	1578	—	560	(2)
*Bs*HemAT (FeII)	1352	1469	1558	225	—	
O_2-*Ec*DosC-heme	1377	1499	1581	—	565	(28)
*Ec*DosC-heme (FeII)	1353	1470	1564	227	—	
O_2-*Af*GcHK	1375	1501	1579	—	557	(29)
*Af*GcHK (FeII)	1354	1470	1558	223	—	
O_2-*Rm*FixL*	1376	1502	1577	—	n.d.	(62)
*Rm*FixL* (FeII)	1355	1470	1558	212	—	
*Rr*CooA (FeII)	1359	1491	1579	n.d.	—	(67, 68)
sGC (FeII)	1358	1471	1562	204	—	(13, 65)

Error is $2\,cm^{-1}$.

*Af*GcHK, globin-coupled histidine kinase from *Anaeromyxobacter sp.* Fw109-5; *Av*GReg and *Av*GReg-Gb, *in vivo*-folded *A. vinelandii* full-length and truncated globin-coupled regulator; †*Av*GReg and †*Av*GReg178, *in vitro*-refolded *A. vinelandii* full-length and truncated globin-coupled sensor; b, broad peak; *Bpe*GReg and *Bpe*GReg*, globin-coupled sensor from *B. pertussis* wild-type and with mutated cysteines (Cys16, 45, 114, 154); *Bpe*GReg-Gb and *Bpe*GReg-Gb*, isolated globin domain of *Bpe*GReg and *Bpe*GReg*; *Bs*HemAT, heme-based aerotaxis transducer from *Bacillus subtilis*; DGC, diguanylate cyclase; *Ec*DosC-heme, isolated heme-binding domain from *Ec*DosC, a globin-coupled sensor with DGC activity from *Escherichia coli*; n.d., not detected; *Rm*FixL*, soluble truncated domain of the *Rhizobium meliloti* nitrogen fixation gene expression regulator; *Rr*CooA, *Rhodospirillum rubrum* carbon monoxide oxidation activator; sGC, soluble guanylyl cyclase; *Sw*Mb, sperm whale myoglobin.

This is also found for the deoxy form of horse heart Mb ($302\,cm^{-1}$) (25). In both cases, O_2 ligation causes a reduction of the out-of-plane distortion (less pronounced γ_7 mode). A similar trend is observed for the γ_7 bending modes of *Bpe*GReg(-Gb) (Fig. 1C).

The heme propionate and vinyl modes reveal important information about the stabilization of the heme by the surrounding protein. The vinyl $\delta(C_\beta C_a C_{b2,4})$ bending modes more or less coincide and give rise to broadened peaks around 421, 414, and $417\,cm^{-1}$ for O_2-*Bpe*GReg-Gb, O_2-*Bpe*GReg*, and O_2-*Bpe*GReg-Gb*, respectively (Fig. 1C.c and Supplementary Fig. S1A.a, A.c). This indicates that the out-of-plane distortions influence each of the pyrrole units in a similar way (68). The increase in wavenumber of this mode for the globin domain compared with the full-length domain indicates an effect of the transmitter domain on the globin domain.

This effect was not observed for the *Av*GReg proteins ($415\,cm^{-1}$) (Fig. 1A.a, A.c). Deoxygenation leads for *Bpe*GReg* and *Bpe*GReg-Gb* to $\delta(C_\beta C_a C_{b2,4})$ bending modes at $412\,cm^{-1}$, whereby the peaks are clearly less broad than in the case of the oxygenated proteins (Fig. 1C and Supplementary Fig. S1). This means that O_2 ligation influences the stabilization of the two vinyl groups in a different way. Again, this effect is far less pronounced in the *Av*GReg case (Fig. 1A).

O_2-*Av*GReg and O_2-*Av*GReg-Gb display the $\delta(C_\beta C_c C_d)$ propionate bending mode at 381 and $377\,cm^{-1}$, respectively (Fig. 1A.a, A.c), whereas those of O_2-*Bpe*GReg-Gb, O_2-*Bpe*GReg*, and O_2-*Bpe*GReg-Gb* are found at 382, 375, and $378\,cm^{-1}$, respectively (Fig. 1C.c and Supplementary Fig. S1A.a, A.c). This suggests a moderate-to-strong electrostatic interaction of the heme propionate groups with the surrounding amino acid side chains. Interestingly, the $\delta(C_\beta C_c C_d)$ mode is found at $363\,cm^{-1}$ for ferrous *Av*GReg and $380\,cm^{-1}$ for ferrous *Av*GReg-Gb. The former low value reflects the pronounced effect of the second domain on the heme surrounding upon ligand binding. While this mode is still clearly detectable for the deoxy ferrous state of *Av*GReg(-Gb) (Fig. 1A.b, A.d), the $\delta(C_\beta C_c C_d)$ mode can only be weakly observed for deoxy ferrous *Bpe*GReg-Gb (Fig. 1C.d, small peak at $379\,cm^{-1}$).

For the *in vivo*-folded O_2-*Av*GReg and O_2-*Av*GReg-Gb, two $\nu_{Fe\text{-}O2}$ modes were found (Fig. 1A.b, A.d and Table 2). The first mode is located at $563\,cm^{-1}$ ($561\,cm^{-1}$), whereas the

second mode is located at 573 cm^{-1} (see Supplementary Fig. S2 for details of this spectral region in the RR spectrum of O_2-*Av*GReg).

The 573 cm^{-1} mode is similar to the one observed for other globins, such as Mb, which show $\nu_{Fe\text{-}O2}$ around 570 cm^{-1} (12, 24, 27, 58). Lower Fe-O_2 stretching modes of 557–560 cm^{-1} have been found for the oxygenated forms of *Bs*HemAT (2) and *Af*GcHK (29) (Table 2). In this respect, previous studies on *Mycobacterium tuberculosis* (74) and *Chlamydomonas eugametos* 2/2Hbs (11) indicate that the low $\nu_{Fe\text{-}O2}$ mode is related to a strong hydrogen bond between the bound O_2 molecule and residue TyrB10. As such, this low $\nu_{Fe\text{-}O2}$ mode suggests a strong stabilization of the bound O_2 through hydrogen bonding in *Av*GReg, whereas the 573 cm^{-1} indicates the coexistence of a more open configuration in which the O_2 is not stabilized.

For the oxygenated *Bpe*GReg* variants, only a $\nu_{Fe\text{-}O2}$ mode in the 556–560 cm^{-1} region is found (Table 2, Fig. 1, and Supplementary Fig. S1), indicating that the O_2 ligand is strongly hydrogen bonded to distal amino acids with no open conformation present. This will be shown to correlate with the kinetics data. A very recent Fourier transform infrared (FTIR) study on the carbon monoxide (CO)-ligated ferrous *Bpe*GReg and its Tyr43Phe variant revealed that one of the CO-bound conformers is strongly hydrogen bonded to the distal Tyr(43)B10, in line with the here observed H-bonding of the O_2 ligand (51).

In earlier work, we already performed RR analyses on †*Av*GReg(-Gb) (64). While the RR data obtained in both studies are similar for the globin domain of the protein, the RR and electron paramagnetic resonance data of †*Av*GReg showed the protein to be in the ferric form due to the *in vitro* refolding. Supplementary Figure S3 shows the optical absorption and RR data for *Av*GReg oxidized with ferricyanide. It shows that (partial) oxidation of the protein can be obtained chemically but that it also leads to partial denaturation of the protein as can be derived from the optical absorption peak at 646 nm. The spectra in Supplementary Figure S3 for oxidized *Av*GReg agree with those previously obtained for †*Av*GReg, where also signs of partial denaturation were found (64).

Ligand binding kinetics on Av*GReg proteins*

*Av*GReg proteins and the *Av*GReg YB10F mutant were characterized in terms of the CO and O_2 binding equilibria and their kinetics as described in the Materials and Methods section. In the whole CO concentration range explored in the flash-photolysis experiments, the time courses of the CO binding to *Av*GReg can be described by a single exponential, allowing the use of a minimum reaction mechanism (Scheme 1, Materials and Methods section) (64). The value of the kinetic parameter that defines CO binding [$k'_{CO} = (0.48 \pm 0.01) \times 10^6\ M^{-1} \cdot s^{-1}$] is very similar to the value reported for *Sw*Mb (Table 3 and Fig. 2). Only a minor influence is noticed of the protein truncation or YB10F mutation. However, the other GCSs characterized to date show a very moderately (*Bs*HemAT) to significantly lower (*Ec*DosC and *Af*GcHK) CO association rate constant (Table 3).

The results of the flash-photolysis O_2/CO competition experiment can be described with a second-order reaction mechanism (see the Materials and Methods section, Scheme 2). The O_2 association/dissociation rate constants of *Av*GReg, as well as the constant for CO dissociation from *Av*GReg (Table 3 and Fig. 2C, D), have been determined using Equations (1) and (2) (see the Materials and Methods section). Interestingly, stopped-flow measurements reveal the presence of a second phase in the O_2/CO replacement mechanism (Table 3 and Fig. 2B). Therefore, we can conclude that *Av*GReg is characterized by a fast O_2 binding [$k'_{O2} = (12.2 \pm 1.5) \times 10^6\ M^{-1} \cdot s^{-1}$] and two O_2 dissociation constants [$k_{O2} = (1732 \pm 377)\ s^{-1}$ and $k_{O2} = (0.53 \pm 0.05)\ s^{-1}$].

The O_2 association and dissociation rate constants we present here for the *Av*GReg differ significantly from the ones measured previously for the *in vitro* refolded protein †*Av*GReg (Table 3). In particular, †*Av*GReg appears to release dioxygen 160 times slower (high k_{O2}) and 1.3 times faster (low k_{O2}).

Table 3. Kinetics and Equilibrium Constants for Ligand Binding to Some Hemoproteins

	CO	*O_2*			
Hemoprotein	k'_{CO} (10^6 $M^{-1} \cdot s^{-1}$)	k'_{O2} (10^6 $M^{-1} \cdot s^{-1}$)	k_{O2} (s^{-1})	$K_d = \frac{k_{O2}}{k'_{O2}}$ (10^{-6} M)	*References*
*Av*GReg	0.48 ± 0.01	12.2 ± 1.5	1732 ± 377, 0.53 ± 0.05	141, 0.04	This study
*Av*GReg-Gb	0.20 ± 0.01	—	—	—	This study
*Av*GRegYB10F	0.31 ± 0.01	20.2 ± 1.3	18,389 ± 556, 166 ± 18	910, 8.22	This study
*Bpe*GReg	0.60 ± 0.01, 0.01 ± 0.01	24.02 ± 1.5	4.0 ± 0.1	0.17	This study
*Bpe*GReg-Gb	0.11 ± 0.01	—	—	—	This study
†*Av*GReg	1	—	10.6, 0.73	—	(64)
†*Av*GReg178	1	424, 5.2	10.6, 0.13	0.025, 0.025	(64)
*Gs*GCS^{162}	6.80	—	23	—	(45)
*Bs*HemAT	0.34	19	1900, 87	100, 4.6	(75)
*Bpe*GReg	1.03, 0.12	7.0	4.5	0.64	(70)
*Ec*DosC	0.22	0.9	13	14	(28)
*Ec*DosC-heme	0.40	1.4	22	16	(28)
*Af*GcHK	0.05	1.3, 0.15	0.10	0.08, 0.67	(29)
*Bj*FixL	—	0.14	20	140	(22)
*Sw*Mb	0.50	14	11	1.27	(5, 21)

*Av*GRegYB10F, mutant of the two proteins in which the Tyr(44) at position B10 is replaced by Phe; *Bj*FixL, *Bradyrhizobium japonicum* nitrogen fixation gene expression regulator; *Bpe*GReg and *Bpe*GReg-Gb, full-length and truncated globin-coupled sensor from *B. pertussis*; *Gs*GCS^{162}, sensor domain from the *Geobacter sulfurreducens* globin-coupled sensor.

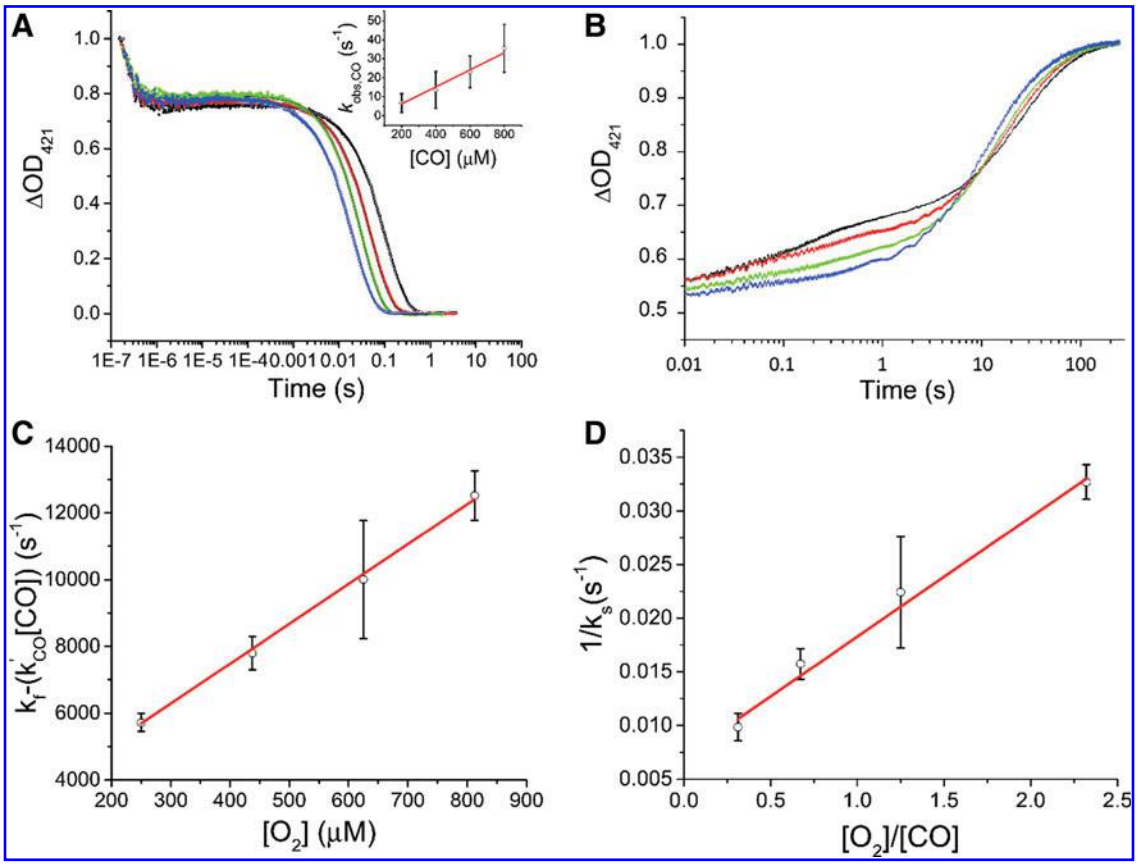

FIG. 2. Ligand binding kinetics curves for *Av*GReg. (A) Experimental curves of the CO-rebinding to *Av*GReg (*black*: 200 μM CO, *red*: 400 μM CO, *green*: 600 μM CO, *blue*: 800 μM CO). The dependence of the pseudo-first order constants of CO binding (k_{obsCO}) to *Av*GReg on the relative ligand concentration is reported in the *inset*. **(B)** Stopped-flow O_2/CO replacement experimental curves of *Av*GReg (*black*: 50% CO–50% O_2, *red*: 60% CO–40% O_2, *green*: 70% CO–30% O_2, *blue*: 80% CO–20% O_2). The fast and the slow replacement phases are detectable for all the gas ratios used. **(C)** Dependence of the apparent k_f constants of O_2 binding to *Av*GReg on the relative ligand concentration. **(D)** Dependence of the apparent k_s constants of CO binding to *Av*GReg on the relative ligand concentration. Experimental values are reported with *open circles*, whereas the theoretical ligand-binding mechanism is represented with a *straight line*. CO, carbon monoxide. Color images are available online.

While two distinct k'_{O2} values were measured for *Af*GcHK (29), a biphasic O_2 dissociation was observed for *Bs*HemAT (75) as for *Av*Greg (Table 3). A difference of more than 200-fold is revealed when comparing the higher K_d values of *Av*GReg and *Af*GcHK, whereas the lower K_d values are in the same order of magnitude for the two GCSs. This indicates the presence of an extremely stable Fe-O_2 complex in both cases. In contrast, we find that the higher K_d values of *Av*GReg and *Bs*HemAT are in the same order of magnitude, whereas the lower K_d of *Av*GReg is 100 times smaller than that of *Bs*HemAT. The latter observation highlights the very high O_2 affinity of *Av*GReg, being the highest among the other globin sensors characterized to date, suggesting that it can be (and remain) activated in the presence of traces amounts of O_2.

A likely explanation of these results lies in the observation of two $\nu_{Fe\text{-}O2}$ modes for O_2-ligated *Av*GReg in solution, linked to an open and closed conformation for the O_2 stabilization, responsible for the two dissociation constants, similarly as for *Bs*HemAT (75). Within this model, when the globin domain is in the open conformation, O_2 is less stabilized inside the heme pocket, allowing a more efficient diffusion of CO from the outer environment, and faster O_2 displacement. However, in the closed conformation, O_2 is firmly bound in the heme pocket and well protected from the solvent. The competition between O_2 and CO is impaired; thus, O_2 displacement is significantly slower.

The results for *Av*GRegYB10F indicate that Tyr(44)B10 plays an important role in this regulation (Table 3 and Supplementary Fig. S4). Not only does the fastest O_2 dissociation rate increase with an order of magnitude upon mutation but also the dissociation rate from the closed confirmation increases with a factor of ~ 300.

Ligand binding kinetics on B. pertussis *proteins*

The ligand binding parameters for CO and O_2 binding to *Bpe*GReg and *Bpe*GReg-Gb are summarized in Table 3 and Figure 3. Interestingly, the CO binding reactions of *Bpe*GReg and the isolated *Bpe*GReg-Gb show a different decay. The double exponential rebinding to *Bpe*GReg is defined with $k'_{COfast} = 0.60\ \mu M^{-1} \cdot s^{-1}$ and $k'_{COslow} = 0.01\ \mu M^{-1} \cdot s^{-1}$, whereas the rate constant of the *Bpe*GReg-Gb single exponential reaction is $k'_{CO} = 0.11\ \mu M^{-1} \cdot s^{-1}$. The explanation for this difference must be related to the presence of the transmitter domain, although we believe that it goes beyond the mere structural effect of the absence/presence of this domain, as no major modification of the heme environment can be ascribed to the isolated globin domain.

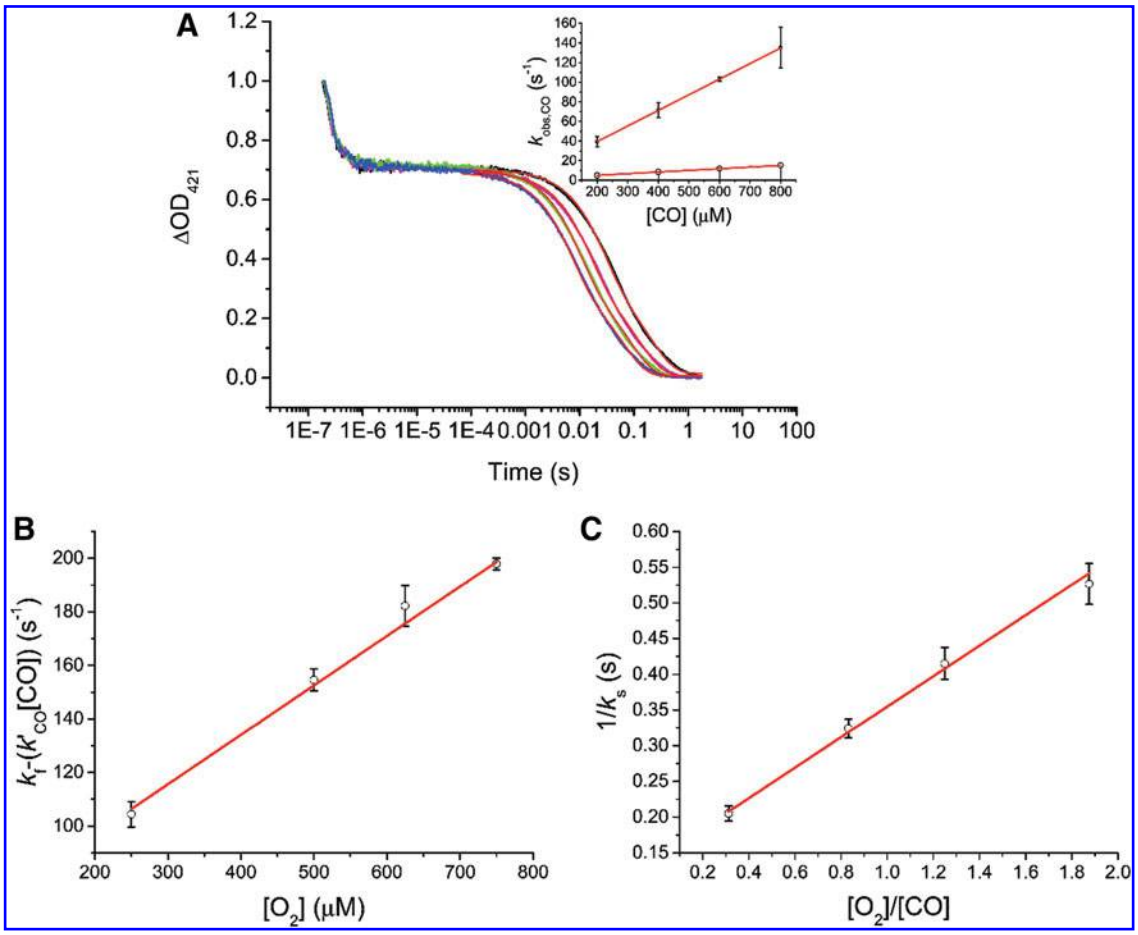

FIG. 3. Ligand binding kinetics curves for *Bpe*GReg. (A) Experimental CO-rebinding decays to *Bpe*GReg (*black*: 200 μM CO, *magenta*: 400 μM CO, *green*: 600 μM CO, *blue*: 800 μM CO) with the corresponding fitting curves (in *red color*). The dependence of the second-order constants of CO binding (k_{obsCO}) to *Bpe*GReg on the relative ligand concentration is reported in the *inset*. Experimentally obtained values are indicated with *closed* (fast rebinding) and *open* (slow rebinding) *circles*, the theoretical fitting lines are reported in *red*. **(B)** Dependence of the apparent k_f constants of O_2 binding to *Bpe*GReg on the relative ligand concentration. **(C)** Dependence of the apparent k_s constants of CO binding to *Bpe*GReg on the relative ligands concentration ratio. Experimental values are reported with *open circles*, whereas the theoretical ligand-binding mechanism is represented with *red lines*. Color images are available online.

Considering also the dimerization process, we confirm the data by Rivera *et al.* (50) that the intra- and intermolecular interactions influence the ligand binding capabilities and therefore result in this CO affinity difference. Surprisingly, recent FTIR of *Bpe*GReg-Gb and *Bpe*GReg showed three CO stretches in both proteins, corresponding to an open and a closed (H-bonded) conformation and a pH-dependent conformer stabilized by structural water (51).

The O_2/CO competition studies and the O_2 association/dissociation rate constants of *Bpe*GReg have been determined for *Av*GReg. With $k'_{O2} = 24.02\ \mu M^{-1} \cdot s^{-1}$ and $k_{O2} = 4.0\ s^{-1}$ (Table 3), *Bpe*GReg is capable of selective and more efficient O_2 binding when a gas mixture is present, as is also the case for myoglobin (1).

Moreover, the low K_d values for O_2 ($K_d = 0.17\ \mu M$) indicate that this sensor will be saturated with O_2 in physiological conditions. This is in line with the RR data that reveal only one $\nu_{Fe\text{-}O2}$ mode agreeing with a strong hydrogen bonding and thus stabilization of the dioxygen ligand. Despite the fact that the reported k'_{O2} from Wan *et al.* (70) is lower, the results are in accordance with the reported transmitter domain activation *via* O_2 binding to the sensor domain (70). Indeed, the very high affinity of the full-length *Bpe*GReg suggests that this characteristic ensures a stable promotion of the *Bpe*GReg DGC activity, resulting in the typical chronic infection-related biofilm persistence (6, 7, 50, 70).

DGC activity of Av*GReg*

We measured and analyzed the DGC activity of *Av*GReg to complement the already published data on *Bpe*GReg (7, 70). By means of an optimized DGC activity assay, we could collect reproducible time point series within few seconds from time zero to confidently determine the initial reaction rate. We tested numerous substrate concentrations, which revealed a high sensitivity of O_2-*Av*GReg to product inhibition, as already reported for *Bpe*GReg and *Ec*DosC (28, 70). To avoid bias due to this effect, we determined the enzyme specificity constant (calculated as k_{cat}/K_m) at GTP concentrations where no product inhibition was detected as described in the Materials and Methods section (Fig. 4) and no cooperativity was seen.

For the oxygenated form of the *in vivo*-folded *Av*GReg, the reaction reached completion after 20 min for all the substrate

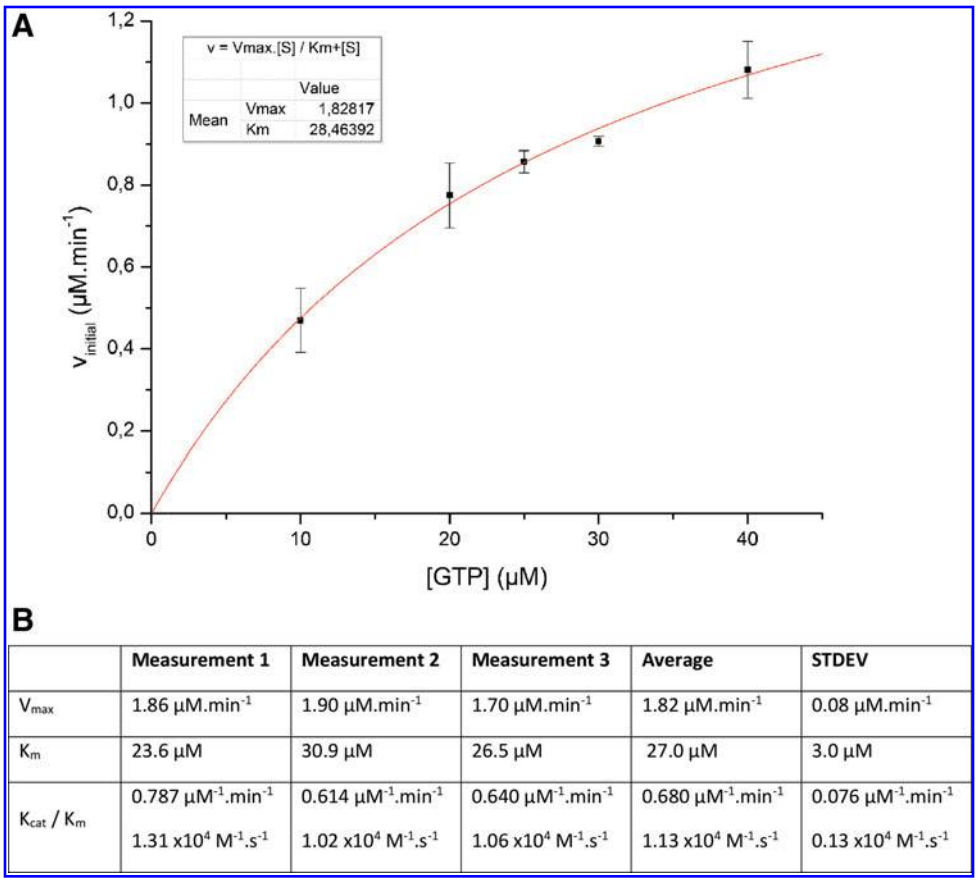

	Measurement 1	Measurement 2	Measurement 3	Average	STDEV
V_{max}	1.86 µM.min^{-1}	1.90 µM.min^{-1}	1.70 µM.min^{-1}	1.82 µM.min^{-1}	0.08 µM.min^{-1}
K_m	23.6 µM	30.9 µM	26.5 µM	27.0 µM	3.0 µM
K_{cat} / K_m	0.787 µM^{-1}.min^{-1} 1.31 x10^4 M^{-1}.s^{-1}	0.614 µM^{-1}.min^{-1} 1.02 x10^4 M^{-1}.s^{-1}	0.640 µM^{-1}.min^{-1} 1.06 x10^4 M^{-1}.s^{-1}	0.680 µM^{-1}.min^{-1} 1.13 x10^4 M^{-1}.s^{-1}	0.076 µM^{-1}.min^{-1} 0.13 x10^4 M^{-1}.s^{-1}

FIG. 4. Enzymatic characteristics of the DGC activity of *Av*GReg. (**A**) Reaction rate. (**B**) Summary of three independent measurements. DGC, diguanylate cyclase. Color images are available online.

concentrations used (20–65 μM GTP) (data not shown), yielding a k_{cat}/K_m value of $(1.13 \pm 0.13) \times 10^4\ M^{-1} \cdot s^{-1}$. O_2-*Bpe*GReg shows a 66-fold lower enzyme specificity as published by Burns *et al.* ($k_{cat}/K_m = 0.17 \times 10^3\ M^{-1} \cdot s^{-1}$) (6) with completion reached after 30 min, whereas *Ec*DosC is characterized by a high autoxidation rate that hindered the estimation of the exact turnover number (28).

The ferrous-unligated form of *Av*GReg was also assayed for the DGC activity. Comparison of the O_2-*Av*GReg and unligated *Av*GReg catalyzed reactions showed that in the latter case c-di-GMP synthesis is 50% decreased (Fig. 4), as previously reported also for *Bpe*GReg and *EcDosC* (28, 70). These results confirm the role of O_2 as DGC reaction triggers for this class of GCSs. Considering that *A. vinelandii* does not grow anaerobically and the very high O_2 affinity of *Av*GReg, it is likely that in physiological condition the *Av*GReg sensor is in the O_2-bound active state already in the presence of traces amounts of O_2.

Tertiary and quaternary structures of Av*GReg-Gb and* Bpe*GReg-Gb**

The ferric aquo-met form of *Av*GReg-Gb and *Bpe*GReg-Gb* crystal structures has been determined at 2.83 Å and 3.20 Å resolution, respectively (two molecules per asymmetric unit, referred to as A and B in both cases). The final *Av*GReg-Gb model consists of 258 amino acids; no electron density is observed for residues 48–67 and 46–69 in chains A and B, respectively (B-C-E region). The refined *Bpe*GReg-Gb* structure comprises 306 amino acids; only residues 57–63 in chains B (C-E loop) show poor electron density. Data collection and refinement statistics are reported in Table 4.

The overall fold of *Av*GReg-Gb and *Bpe*GReg-Gb* conform to the modified globin fold typically found for GCS sensor domains (45, 63, 75) and protoglobin (40, 46, 47), consisting of eight helices, which, according to the classical globin nomenclature, have been named in alphabetical order from A to H, with a Z helix preceding the A at the N-terminus and the D helix absent (Fig. 5A, B). The two *Av*GReg-Gb and *Bpe*GReg-Gb* structures superimpose well, with a root mean squared deviation (rmsd) of $\sim$1.3 Å over 126 Cα atom pairs, with structural differences localized at the N-terminal region (including the Z helix), in the B-E region, and in the EF and GH loops (Fig. 5C).

Overall, two major features, both associated to the heme pocket, uniquely characterize *Av*GReg-Gb. On the heme proximal side, *Av*GReg-Gb exhibits one of the longest F-helix seen in globins (23 residues); this is due to the fact that the N-terminus of the F helix contains one more turn at the expense of the C-terminal turn of the E helix (Fig. 5A, C). On the heme distal side, the structural disorder at the B-C-E region (in both the A and B chains) results in the unwinding of almost the whole B-helix (Fig. 5A). The B-C-E region is instead well structured in *Bpe*GReg-Gb* (Fig. 5B, C).

The *Av*GReg-Gb and *Bpe*GReg-Gb* monomers assemble in homodimers with the interface residues belonging to the Z, G, and H helices of both A and B chains (Fig. 6A, B). Thus, the dimerization interface has a four α-helical G-H bundle as the core region (including 11 H-bonds and 7 salt bridges for

TABLE 4. DATA COLLECTION AND REFINEMENT STATISTICS

Data collection	Av*GReg-Gb*	Bpe*GReg-Gb**	Bpe*GReg-Gb**-2*
Space group	$P2_1$	$C2$	$C2$
Cell dimensions			
a, *b*, *c* (Å)	47.9, 49.5, 62.8	105.0, 86.7, 41.8	70.0, 53.1, 81.2
α, β, γ (°)	90.0, 91.8, 90.0	90.0, 93.3, 90.0	90.0, 93.2, 90.0
Resolution (Å)	30.5–2.83 (2.98–2.83)[a]	52.4–3.20 (3.37–3.2)	42.3–1.55 (1.63–1.55)
No. of reflections	22,497	17,105	145,853
Unique reflections	6845	6186	42,168
R-merge[b] (%)[a]	9.3 (49.8)	24.6 (52.7)	6.8 (49.8)
I/σ(I)[a]	8.6 (2.5)	3.4 (2.0)	9.8 (2.7)
Completeness (%)[a]	95.8 (97.7)	99.2 (99.5)	97.6 (97.5)
Multiplicity[a]	3.3 (3.4)	2.8 (2.8)	3.5 (3.5)
Refinement statistics			
R-factor[c]/R-free (%)	25.5/29.7	20.9/24.0	15.6/20.4
Protein residues	258 (A: 6–47, 68–157), (B: 7–45, 70–156)	306 (A:3–157), (B: 3–56, 61–157)	307 (A: 5–158), (B: 3–155)
Heme groups	2	2	3
Water molecules	4	30	171
Glycerol molecules	—	—	2
Imidazole molecules	—	—	1
rmsd from ideality			
Bond lengths (Å)	0.011	0.010	0.017
Bond angles (°)	1.97	1.45	1.81
Ramachandran plot (%)			
Most favored	88.1	92.3	98.7
Additionally allowed	11.9	7.7	1.3
Disallowed regions	0.0	0.0	0.0

[a]Highest resolution shell parameters are in parentheses.
[b]R-merge = $\Sigma_h\Sigma_i \mid I_{hi} - \langle I_h \rangle \mid / \Sigma_h\Sigma_i I_{hi}$.
[c]R-factor = $\Sigma_h \mid\mid F_{obs}\mid - \mid F_{calc}\mid\mid / \Sigma_h \mid F_{obs}\mid$, with F_{obs} being the observed and F_{calc} the calculated structure factor amplitudes.
rmsd, root mean squared deviation.

*Av*GReg-Gb, and 11 H-bonds and 16 salt bridges for *Bpe*GReg-Gb*), whereas the adjacent Z helices provide mostly van der Waals interactions.

The dimeric assembly observed in *Av*GReg-Gb and *Bpe*GReg-Gb* is similar to those found in (sensor domain from the Geobacter sulfurreducens globin-coupled sensor [*Gs*GCS[162]] (PDB code: 2W31) (45), *Bs*HemAT (PDB codes: 1OR4, 1OR6) (75), *Ec*DosC (PDB code: 4ZVA, 4ZVB) (63), and *Ma*Pgb (PDB codes 2VEB, 2VEE) (40). However, the dimeric interface surface area can vary significantly: it is large for *Ma*Pgb (~2100 Å^2), *Bs*HemAT (~1800 Å^2), and *Gs*GCS[162] (~1700 Å^2); medium for *Ec*DosC (~1300 Å^2) and *Av*GReg-Gb (1304 Å^2); and only 1042 Å^2 for *Bpe*GReg-Gb*.

Furthermore, the precise orientation of the A/B subunits in the dimer is not the same in different GCS proteins. Indeed,

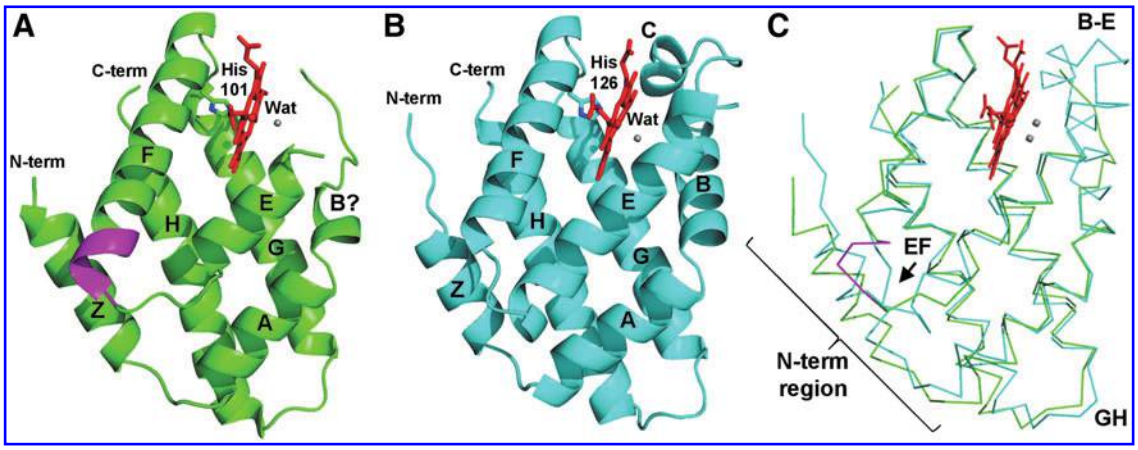

FIG. 5. Tertiary structures. Ribbon representation of the tertiary structure of **(A)** *Av*GReg-Gb (*green*) and **(B)** *Bpe*GReg-Gb* (*cyan*). Helices are labeled accordingly with the globin fold nomenclature. The extra-turn of the F helix of *Av*GReg-Gb is shown in *magenta*. Proximal His residues and Fe^{3+}-ligated water molecules are indicated. **(C)** Cα-trace overlay of the *Av*GReg-Gb A (*green*) and *Bpe*GReg-Gb* (*cyan*). Regions displaying the main structural differences are indicated by labels. *Bpe*GReg-Gb*, *Bpe*GRegGb with cysteines (Cys16, 45, 114, 154) mutated to serines. Color images are available online.

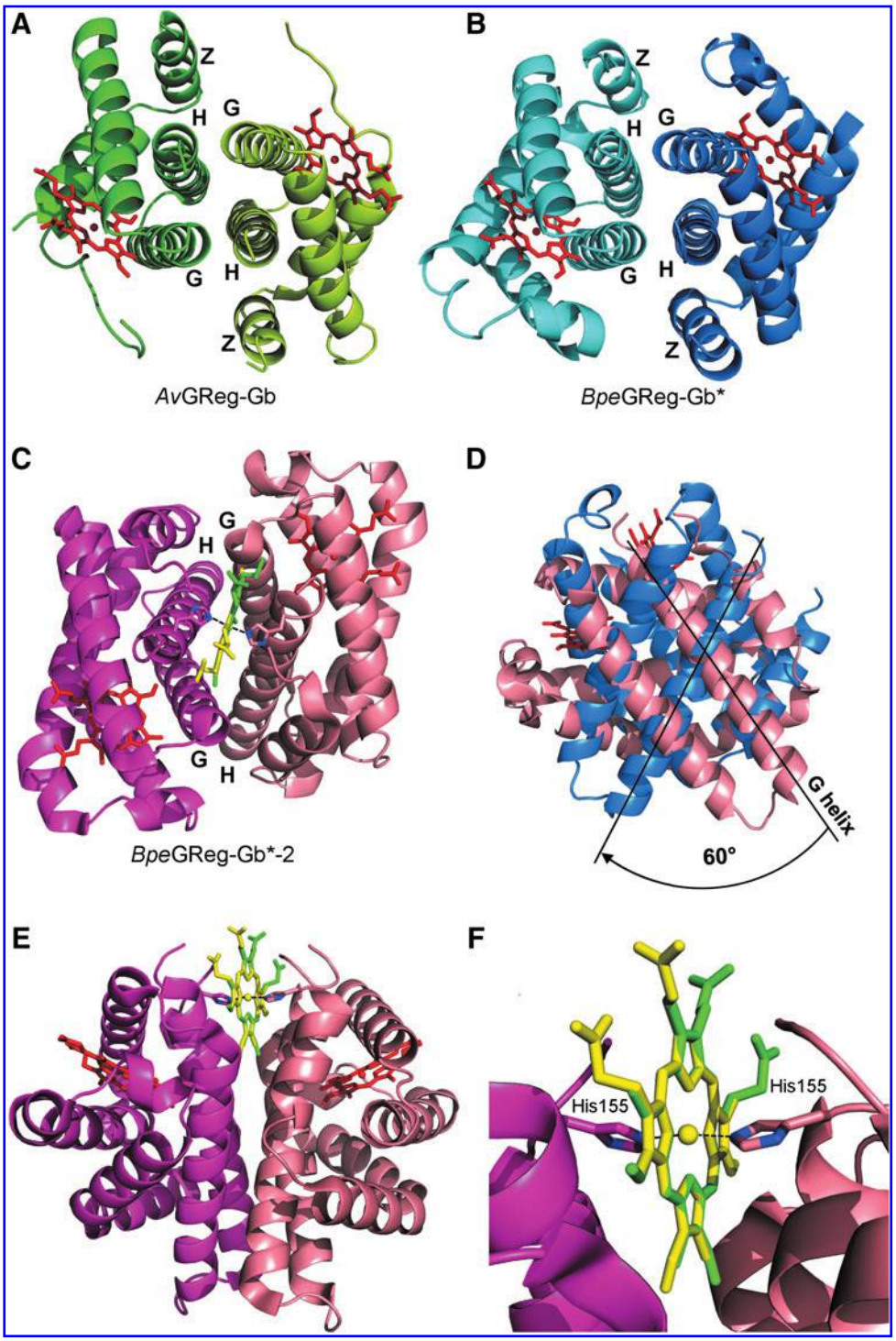

FIG. 6. Quaternary structures. Top view of **(A)** the *Av*GReg-Gb dimer and **(B)** the *Bpe*GReg-Gb* dimer, with the two subunits interacting mainly through the G- and H-helices (helical bundle), shown as ribbon models. The heme groups are shown in *red*. **(C)** Dimeric arrangement of *Bpe*GReg-Gb*-2. The dimeric interface involves the G- and H-helices as in the *Bpe*GReg-Gb* dimer, but the subunits are oriented differently. **(D)** Relative orientation of the B subunits of *Bpe*GReg-Gb* (*blue*) and *Bpe*GReg-Gb*-2 (*pink*), after superimposing the two A chains (omitted in the picture for clarity). The rotation of 60° is indicated, taking the position of the G helices as reference. **(E, F)** The heme group at the *top* of the *Bpe*GReg-Gb*-2 dimer is modeled in two conformations (*green* and *yellow*) with 0.5 occupancy each, with the Fe-atom hexacoordinated to the His155 side chain of the two subunits of the dimer. Color images are available online.

when the *Av*GReg-Gb A chain is superimposed to that from the other GCSs, the match with the B chain is good for *Bpe*GReg-Gb* and *Ec*DosC, whereas the *Bs*HemAT B chain is rotated by ~20°, and *Gs*GCS[162] and *Ma*Pgb by ~30°, around an axis approximatively orthogonal to the G-H helices.

Strikingly, a similar (although more pronounced, ~60°) different orientation of the subunits of the dimer has been found in another *Bpe*GReg-Gb* crystal form (same space-group *C*2, but different unit cell), determined at 1.55 Å resolution (*Bpe*GReg-Gb*-2) (Table 4). This second quaternary structure is symmetrical around a crystal axes, covers a contact surface of 1305 Å^2 (similar to *Av*GReg-Gb and *Ec*DosC) with 14 hydrogen bonds and 10 salt bridges, and involves the Z, G, and H helices, and the CE corner (Fig. 6C, D).

It should be noted that the different dimerization mode cannot be ascribed to a different structure of the interfacing monomers, since the *Bpe*GReg-Gb* and *Bpe*GReg-Gb*-2 structures do not show significant deviations if compared

monomer by monomer (rmsd values ranging between 0.50 Å and 0.80 Å, over 138–145 Cα pairs).

The different quaternary assembly is most likely responsible for the minor structural deviations observed at the N-terminus of the E helix, in the FG, G, GH, and H regions between the *Bpe*GReg-Gb* and *Bpe*GReg-Gb*-2. In particular, the C-terminal His155 residue, buried at the dimeric interface in *Bpe*GReg-Gb*, is solvent exposed in *Bpe*GReg-Gb*-2 and interacting with an additional heme group (probably released in solution by a fraction of *Bpe*GReg-Gb*), which becomes hexacoordinated between the end of two H-helices at the top of the dimeric interface (Fig. 6E, F).

Heme proximal side

*Av*GReg-Gb and *Bpe*GReg-Gb* share a very similar heme pocket proximal side, due to a very high sequence similarity in this protein region. The proximal heme pocket is lined by residues Ile(97)F4, Ile(100)F7, Ile(104), Ile(106), Val(111)G4, and Met(154)H17 in *Av*GReg-Gb, and Val(95)F4, Val(98)F7, Ile(102), Ile(104), Val(109)G4, and Met(153)H17 in *Bpe*GReg-Gb*, which surround and mostly contact the porphyrin ring.

Both *Av*GReg-Gb and *Bpe*GReg-Gb* show a loose coordination bond between the Fe atom and the proximal His residue with Fe–His(101)F8 NE2 distance of 2.39 Å and 2.50 Å in the A and B monomers of *Av*GReg-Gb, and Fe–His(99)F8 distance of 2.10 Å and 2.29 Å in A and B chains of *Bpe*GReg-Gb*. In *Av*GReg-Gb and *Bpe*GReg-Gb*, the F8 imidazole ring lies in a staggered azimuthal orientation relative to the heme pyrrole N-atoms in chain A, and it is eclipsed in chain B along the direction of the heme pyrrole NA-NC atoms in *Av*GReg-Gb and NB-ND in *Bpe*GReg-Gb* (Fig. 7A). In the *Bpe*GReg-Gb*-2, His(99)F8 stabilizes the heme iron atom with a distance of 2.20 Å in chain A and 2.14 Å in chain B, being always eclipsed along the direction of the heme pyrrole NB and ND atoms.

Heme distal side

The heme distal side of *Av*GReg-Gb and *Bpe*GReg-Gb* varies considerably, but both reveal a high conformational flexibility of the B-C-E region. In *Av*GReg-Gb, the heme distal pocket residues Tyr(42)B8, Phe(43)B9, Tyr(44)B10, and Leu(70)E11 surround a heme-ligated water molecule (2.81 Å and 3.32 Å in the A and B chains, respectively), which is not stabilized by any polar interaction provided by the protein (Fig. 7A). It should be noted, however, that part of the heme distal site corresponding to the B-C-E region (residues 48–67 and 46–69 in chain A and chain B, respectively) could not be modeled due to the low connectivity of the experimental electron density map.

In particular, this disordered region involves the C-terminal end of the B-helix, which in *Av*GReg-Gb appears to be almost completely unwound (Fig. 5A). As a consequence, Tyr(44)B10, a conserved residue usually involved in ligand stabilization in GCS proteins, is too far to H-bond the heme-bound water molecule (Fig. 7A). The same considerations hold for the nearby Tyr(42)B8, an amino acid that is instead specific of *Av*GReg-Gb and few others GCSs (19). However, both Tyr residues point their hydroxyl groups toward the interior of the distal site and therefore could be involved in ligand stabilization in the context of a structured B-C-E region.

Conformational disorder at the BE distal site region has been previously reported in GCSs and other globins, and, in some cases, associated to functional roles. For instance, in GCSs and related proteins (*i.e.*, protoglobin), disorder in this region has been associated to multiple conformations of specific residues whose side chain orientations in the heme distal site depend on the ligation state of the heme-Fe atom (40, 45, 46, 47, 75). However, in *Av*GReg-Gb, the disordered region is delimited by residues Gly(40)B6-Pro(41)B7 on one side and Gly(68)E9 on the other, which are specific for *Av*GReg-Gb and not conserved in other GCSs (19, 45).

The *Bpe*GReg-Gb* heme iron atom coordinates to a water molecule (at 3.06 Å in the A chain and at 2.90 Å in the B chain) at the distal site, which is not stabilized by any interaction with the amino acids facing the distal site. In particular, Tyr(43)B10 is pointing its hydroxyl group toward the exterior of the distal site. The distal side residues are hydrophobic [Phe(42)B9, Leu56, Val(61)E3, Leu(65)E7, Met(69)E11] and well defined in the A chain of the dimer, whereas in the B chain, the C-E region (residues 57–60) is partly disordered (Fig. 7B).

Interestingly, the second crystal form, *Bpe*GReg-Gb*-2, shows an Fe-coordination state at the distal site that differs in the A and B chains and from the *Bpe*GReg-Gb* crystal form: the heme-Fe is loosely hexacoordinated to Tyr(43)B10 (3.11 Å) in chain A (Fig. 7C) and to an imidazole molecule (2.12 Å), probably originating from the purification protocol, in chain B, with Tyr(43)B10 swinging out from the distal site due to steric repulsion caused by the imidazole ligand (Fig. 7D).

Overall, we can conclude that the different dimerization mode of *Bpe*GReg-Gb*-2 has an impact in the distal site geometry reshaping, with Tyr(43)B10 able to point inward and outward, in keeping with the previously proposed mechanism whereby the globin domain dimerization leads to conformation(s) of the distal pocket that adjust the position of the hydrogen bonding residues involved in O_2 dissociation kinetics (50). Interestingly, the distal site swinging movement of TyrB10 has been suggested as the mechanism of O_2 stabilization for other GCSs, as *Bs*HemAT (75) and *Ec*DosC (63).

In *Bpe*GReg-Gb* the heme group's propionates are not interacting with Lys(64)E6 at the distal site nor with Lys(94)F3 at the proximal site (Fig. 7A), whereas in the *Bpe*GReg-Gb*-2 structure, only a loose interaction is present with Lys(64)E6 (Fig. 7C, D).

Discussion

A. vinelandii and *B. pertussis* are highly interesting bacterial systems. Indeed, *A. vinelandii* fixes N_2 in the presence of O_2, a unique metabolic feature that renders it particularly appealing for industrial applications, whereas *B. pertussis* is a highly contagious human pathogen that still causes many deaths worldwide and is therefore of considerable medical interest. In addition, the GCS of both systems are involved in biofilm formation. In this respect, their characterization, here presented, is significant for a more detailed understanding of the control that the sensors might exert on biofilm formation.

The combination of biochemical techniques applied in this study provides complementary pictures of *Av*GReg and *Bpe*GReg functional and structural behaviors. We performed our experiment on *in vivo*-folded full-length proteins. It is important to note that in the previously published study on *Av*GReg and *Av*GReg-Gb, both proteins had been purified from inclusion bodies, followed by *in vitro* refolding (64).

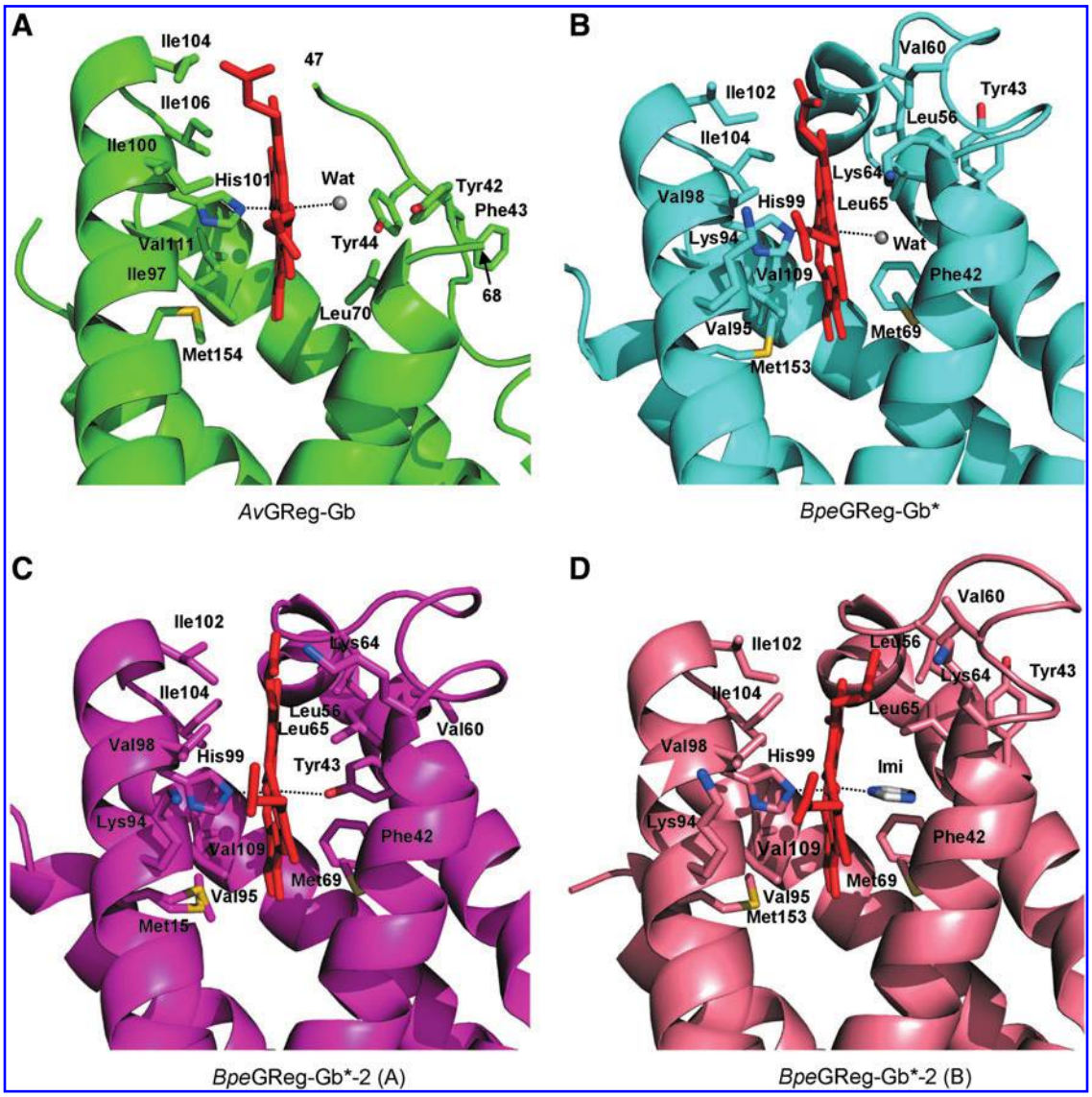

FIG. 7. Proximal and distal sites. The figure shows the main residues building the heme proximal and distal sites for **(A)** *Av*GReg-Gb (A chain), **(B)** *Bpe*GReg-Gb* (A chain), and **(C, D)** *Bpe*GReg-Gb*-2 (A and B chains). The *Av*GReg-Gb and *Bpe*GReg-Gb* distal sites host a water molecule (*gray*) coordinated to the heme-Fe^{3+}. In *Bpe*GReg-Gb*-2, a coordination with Tyr43 is present in the A chain, whereas an imidazole molecule is bound in the B chain. Color images are available online.

The high level of agreement between our data and the optical and RR spectra of the *in vitro*-refolded *Av*GReg-Gb is an indication of the reliability of the refolding method when applied to the globin domain alone. In contrast, the discrepancies detected between *in vivo*-folded *Av*GReg and that purified from inclusion bodies strongly suggest that the presence of the second (transducer) domain may hamper a correct *in vitro* refolding process.

We showed that both the *in vivo*-folded *Av*GReg and *Bpe*-GReg sensors are oxygenated when purified and pentacoordinated when the deoxy ferrous species is produced through dithionite reduction. Additionally, based on our enzymatic *in vitro* assays and the literature, we proved that O_2 binding triggers c-di-GMP biosynthesis and that O_2-*Av*GReg and O_2-*Bpe*GReg are the catalytically competent forms. O_2-*Av*GReg and O_2-*Bpe*GReg display a high sensitivity to product inhibition confirming the literature (70). For O_2-*Av*GReg and O_2-*Bpe*GReg, a k_{cat}/K_m value of $1.13 \pm 0.13 \times 10^4$ $M^{-1} \cdot s^{-1}$ (reported here) and 0.17×10^3 $M^{-1} \cdot s^{-1}$ (6, 7) was obtained, respectively.

The RR measurements indicate that the heme pocket of the fully oxygenated proteins are well structured, with moderate-to-strong electrostatic interactions of the heme propionate groups with the surrounding amino acid side chains and the O_2 molecule tightly bound to the heme-Fe for all forms and an additional more open distal heme-pocket site for O_2-*Av*GReg. These data are confirmed by the recently published structure of the oxygenated form of *Bpe*GReg-Gb (structure not yet released by PDB), where O_2 is described as tightly bound to the Fe^{2+} and H-bonded to Tyr(43)B10, and Lys(64)E6 forms a hydrogen bond with heme propionate (51).

The combination of kinetics measurements and the structural data suggest mechanisms for protein activation and signal transduction. In the case of *Av*GReg, the kinetics measurements reveal a fast O_2 association ($k'_{O2} = 12.2 \times 10^6$ $M^{-1} \cdot s^{-1}$) and a biphasic O_2 dissociation, characterized by fast and slow rates

($k_{O2} = 1732$ and $0.53\ s^{-1}$, respectively). Among GCSs, a biphasic O_2 dissociation has been reported only for *Bs*HemAT (75). The higher K_d for O_2 is in the same order of magnitude for the *Av*GReg and *Bs*HemAT, whereas the lower K_d highlights the very high O_2 affinity of *Av*GReg, being the highest among the other globin sensors characterized to date (Table 3), suggesting that it can be activated in the presence of traces amounts of O_2.

The crucial role of Tyr(44)B10 is highlighted by the binding kinetics study of the YB10F mutant, which shows a significant increase of O_2 dissociation rate, for both the fast and slow rates (Table 3). Specific high-affinity O_2 binding (needed for sensing, transport, and storage) requires significant deviation from the sliding scale rule, which predict that, although the equilibrium dissociation constants (K_d) can vary a lot, the ratios for NO:CO:O_2 binding are roughly the same, namely $1: \sim 10^3: \sim 10^6$ when the proximal ligand is a histidine and the distal site is apolar (66). Indeed, data reported for GCSs (including *Bpe*GReg) show that, in general, CO affinity is higher than O_2 but that the $K_D(O_2)/K_D(CO)$ ratio is much smaller than that predicted by the sliding scale rule due to a preferentially lower $K_D(O_2)$ associated with hydrogen bonding stabilization of the O_2 molecule into the distal site (66).

Within this picture, the biphasic behavior for *Av*GReg O_2 dissociation, measured by flash-photolysis O_2/CO competition, can be explained by the presence of two different *Av*GReg conformations (open and closed, respectively) responsible for the two dissociation rate constants. More precisely, when the globin domain is in the closed conformation, O_2 would be firmly bound in the heme pocket and well protected from the solvent. As a result, the competition between O_2 and CO would be hampered and O_2 displacement significantly slower. On the contrary, when the protein is in the open conformation, O_2 would be less stabilized within the heme pocket, thus allowing a more efficient diffusion of CO from the outer environment and faster O_2 displacement.

Both conformations are in keeping with the RR measurements on the fully oxygenated ferrous *Av*GReg. All in all, the crystal structure of the *Av*GReg-Gb ferric form reveals that the B-C-E region can undergo to structural disorder, probably favored by the Gly-rich sequence at the BE region boundaries (not present in other GCSs), and this protein flexibility is compatible with the presence of an open conformation. From RR and kinetics follows that there is a second more closed (and probably more rigid) conformation that is not populated in the crystals. This closed conformation involves Tyr(44)B10.

Furthermore, the presence of the transmitter domain in the full-length *Av*GReg relaxes the heme proximal coordination when compared with the isolated *Av*GReg-Gb sensor domain. Indeed, the aquo-met crystal structure is in keeping with the RR measurements on the ferrous-unligated protein, indicating a staggered conformation of the proximal His(127)F8 side chain and, therefore, a higher strain on the Fe-His bond for the isolated globin domain relative to the full-length protein. Such relaxation at the F-helix proximal His(127)F8 may be also part of the signal transduction mechanism between domains upon O_2 binding.

In contrast to *Av*GReg, no dramatic change in the sensor domain of *Bpe*GReg can be ascribed to the absence/presence of the transmitter domain. Indeed, the RR spectra measured on *Bpe*GReg-Gb and *Bpe*GReg (and their *Bpe*GReg-Gb* and *Bpe*GReg* Cys-mutants) are very similar. This suggest that the signal transduction mechanism for the *Bpe*GReg globin domain activation involves structural modifications in protein regions far from the heme pocket. The measured k'_{O2} and k_{O2} values suggest that *Bpe*GReg is capable of selective and more efficiently binding O_2 when a gas mixture is present, as is also the case for myoglobin (1). The low K_d (O_2) values indicate that, under physiological conditions, the sensor will permanently bind O_2.

A biphasic behavior for O_2 dissociation, as seen for *Av*GReg, is not recorded for *Bpe*GReg, in line with the RR observation of only one (closed) conformation for the stabilization of the distal O_2 ligand. However, flash photolysis experiments indicate that the CO binding kinetics differs between the isolated *Bpe*GReg-Gb (one exponential) and the full-length *Bpe*GReg (two exponential). This result proves that the overall protein dynamicity changes when the transmitter domain is present, probably due to the presence of structural interactions between sensor and transmitter domains, likely at the oligomerization interface, necessary for the signal transduction process as also seen by Rivera *et al.* (50).

Finally, the crystal structure of the aquo-met form of *Bpe*GReg-Gb* shows that the water ligand is not stabilized by any distal residue, the Tyr(43)B10 hydroxyl group is pointing away from the heme distal side, and the propionates are not interacting with the protein. These data provide a complementary picture of the recently published O_2-bound structure (PDB code: 6M9A) (51) where, instead, the strong O_2-binding to Tyr(43)B10 is coupled with heme distortion, interaction between Lys(64)E6 and the heme propionate, and interaction between Ser(68)E10 and Tyr(43)B10 through a distal water molecule, not present in the *Bpe*GReg-Gb* aquo-met form. Thus, our data support the proposed mechanism that differences in ligation state at the distal side is potentially propagated through interactions with residues on the E helix, allowing for signaling to the DGC output domain.

Furthermore, a second crystal form of ferric *Bpe*GReg-Gb* reveals the presence of two possible dimerization modes, both based on the G-H helical bundle. The first dimerization mode is that typically found in GCSs, the second differs by a rotation of 60° between monomers and is stabilized/forced by the presence of an extra heme molecule, probably due to a somewhat higher heme availability in solution at the more alkaline crystallization condition used (see the Material and Methods section, condition 2), covalently linking two His residues (His155) at the end of the H helices (the region that is linked to the middle domain of the full-length protein). Although this dimerization mode could be classified as a crystallization artifact, it clearly demonstrates that the G-H surface of a monomer is intrinsically characterize by high plasticity, being able to face, fit, and bind its counterpart in more than one way.

The different dimerization mode is also associated with a different distal site organization, with Tyr(43)B10 swinging in and out the distal site. Thus, a transmission mechanism through a partial rotation at the G-H interface is conceivable, whereby a different relative position of the H-helices upon ligand binding would directly affect the following middle domain and/or affect the global oligomerization state of the full-length protein (dimer with low DGC activity *vs.* tetramer with high activity) (51).

Our *in vitro* data on the DGC activity in *Av*GReg demonstrate that O_2-binding to *A. vinelandii* GCS triggers c-di-GMP biosynthesis, as described for *B. pertussis* GCS (20, 33, 51, 70). In bacteria, c-di-GMP is an essential second

messenger involved, *in vivo*, in the regulation (translational and post-translation) of motility, exo-polysaccharide production, and biofilm formation (26, 34, 49, 52). Thus, O_2 binding to GCS as *A. vinelandii* and *B. pertussis* increases c-di-GMP production and activates biofilm formation.

Materials and Methods

Cloning, expression, mutagenesis, and protein purification

Full-length *Av*GReg (472 residues) and its N-terminal globin domain *Av*GReg-Gb (residues 1–170) were amplified by polymerase chain reaction (PCR) and cloned into the pBAD-a vector as previously described (15, 44, 64). In addition, for the *Av*GRegYB10F variant, Tyr(44)B10 was mutated into Phe using the QuickChange™ site-directed mutagenesis method (Stratagene) (14). All were expressed as N-terminal His-tagged proteins in *E. coli* TOP10 cells (Invitrogen) (15, 44) and purified from the soluble fraction using affinity chromatography.

This procedure is very different from the one used to obtain †*Av*GReg in Ref. (64). In that case, the procedure involved the purification of the expressed denatured proteins from inclusion bodies, with a subsequent *in vitro* folding in the presence of hemin. This approach deviates significantly from the here presented method based on *in vivo* folding of the proteins in *E. coli* followed by affinity purification.

Full-length *Bpe*GReg (475 residues) and its N-terminal globin domain (*Bpe*GReg-Gb) (residues 1–169) were amplified by PCR and cloned into the pET23-a vector using *Nde*I and *Xho*I restriction sites. The C-terminal His-tagged fusion proteins were expressed in *E. coli* BL21(DE3)pLysS (Invitrogen) as performed for the *Av*GReg proteins (15, 44).

To prevent aggregation during the crystallization process, four of six cysteine residues present in the globin domain (Cys16, Cys45, Cys114, and Cys154) were mutated into Ser using the QuickChange site-directed mutagenesis method (Stratagene) (14). The selection for the Cys residue to be mutated was carried out based on the *in silico* modeling of *Bpe*GReg-Gb obtained by using the I-TASSER server (72). The mutated proteins are further termed as *Bpe*GReg* (full-length molecule) and *Bpe*GReg-Gb* (globin domain). The *Av*GReg proteins were kept in 50 m*M* Tris-HCl, pH 7.5, 50 m*M* NaCl, 10 m*M* $MgCl_2$, and 5% glycerol, whereas the *Bpe*GReg proteins were kept in 20 m*M* Tris-HCl, pH 8, 50 m*M* NaCl, and 40% glycerol. Both the globin domains were kept in 50 m*M* Tris-HCl, pH 8.5, 10 m*M* NaCl, and 0.5 m*M* EDTA.

UV/Vis absorption spectroscopy

The optical absorption measurements were obtained by using a Varian Cary 5E UV-Vis-NIR spectrometer. The spectra were recorded from 350 to 750 nm at room temperature. The ferrous O_2-ligated forms were measured, without additional treatment (as-purified), soon after protein purification, whereas the unligated form was obtained by adding 1% v/v sodium dithionite saturated solution to the sample, after N_2 bubbling.

RR spectroscopy

The RR spectra were measured on a Dilor XY-800 Raman spectrometer in low-dispersion mode, associated to a liquid N_2-cooled CCD detector (slit width = 200 μm), with a Kr^+ laser operating at 413.1 nm as the excitation source (BeamLok 2060; Spectra-Physics). The applied laser power was 10 mW (*Bpe*GReg proteins) and 15 mW (*Av*GReg variants). The samples had a final concentration of 40 μM and were magnetically stirred at 500 rpm to avoid local heating and photochemical decomposition. Six spectra were recorded with 120–180 s integration time, depending on the protein sample. To remove spikes due to cosmic rays, the highest and lowest data points for each frequency value were removed and averaged over the remaining values with an in-house written program.

Ligand binding kinetics and data analysis

Laser flash photolysis experiments were performed to measure the CO and O_2 binding kinetics at 20°C using a laser photolysis system (Edinburgh Instruments LP920) equipped with a frequency-doubled, Q-switched Nd:YAG laser (Quanta-Ray; Spectra-Physics). A laser flash of 532 nm was used.

The CO–ferrous Hb complexes were prepared in sealed 4×10 mm quartz cuvettes with 1 mL of 100 m*M* potassium phosphate buffer (pH 7.0) containing 1 m*M* EDTA. The buffer was equilibrated with mixtures of CO and N_2 in different ratios to obtain CO concentrations of 50–800 μM by using a gas mixer (HighTech System; Bronkhorst). Saturated sodium dithionite solution (10 μL) was added, and the protein was injected to a final concentration of ~ 4 μM. Formation of the CO–ferrous Hb complex was verified by UV/visible absorption spectroscopy. Recombination of the photodissociated CO ligand was monitored at 418 nm (*Bpe*GReg) or 421 nm (*Av*GReg).

O_2/CO competition studies were performed with the ferrous oxygenated (as-purified) form of the GCS. Sealed cuvettes containing 100 m*M* phosphate buffer, pH 7.0, were flushed with O_2/CO mixtures (O_2 concentrations between 250 and 812.5 μM, and CO concentrations between 350 and 800 μM). The protein was added to the experimental cuvettes immediately before the photolysis experiment. The CO/O_2 displacement was followed at 418 and 436 nm for *Bpe*GReg and at 421 and 436 nm for *Av*GReg.

The data obtained were analyzed with MATLAB® (The MathWorks, Inc., Natick, MA) and fitted with Origin (OriginLab, Northampton, MA). The time courses for CO rebinding followed a monoexponential decay and were fitted to the minimum reaction mechanism (Scheme 1) with equations as described elsewhere (42, 64).

$$GCS + CO \underset{k_{CO}}{\overset{k'_{CO}}{\rightleftarrows}} GCS - CO \qquad \text{(Scheme 1)}$$

The O_2/CO competition time courses fitted with a two-exponential process (Scheme 2) (42), valid also for the globin domain alone:

$$GCS - O_2 + CO \overset{k'_{CO}, k_{O2}}{\rightarrow} GCS - CO + O_2 \qquad \text{(Scheme 2a)}$$

$$GCS + O_2 \overset{k'_{O2}}{\rightarrow} GCS - O_2 \qquad \text{(Scheme 2b)}$$

The values of k'_{O2}, k_{O2}, and k'_{CO} were obtained according to the equations:

$$k_f = k'_{O2}[O_2] + k'_{CO}[CO] + k_{O2}, \quad (1)$$

$$k_s = \frac{k_{O2}}{1 + \frac{k'_{O2}[O_2]}{k'_{CO}[CO]}}, \quad (2)$$

where k_f is the fast observed reaction constant k_{obs}, and k_s is the slow k_{obs} at a given ligand concentration.

The slower O_2 dissociation rate constant was determined with a ligand replacement method using stopped flow, as already described (41). Experiments were performed at 20°C in triplicates on an Applied Photophysics SX20 stopped-flow spectrometer apparatus equipped with the Pro-Data™ software suite. After measurements, the raw data were further analyzed with Origin (OriginLab). The oxygenated protein solution was rapidly mixed with an O_2/CO mixture (the final protein concentration after mixing was 2.5 μM) in 100 μM potassium phosphate buffer, pH 7.5, 1 m*M* EDTA.

DGC assay

A HPLC-based DGC assay was adapted from Ref. (54) and performed in triplicate to quantify c-di-GMP synthesis by *Av*GReg. Shortly, 10 μM of enzyme was incubated at 37°C with 20–65 μM GTP in 50 m*M* Tris-HCl, pH 7.5, 50 m*M* NaCl, and 10 m*M* $MgCl_2$. Aliquots were taken at different times, and the reaction was rapidly stopped with one-fourth volume of 0.5 *M* EDTA, pH 8.0, which ensures repeatability in the measurement of more time points in a few seconds time frame, as required for initial rate determination of enzymatic processes.

For deproteination, the stopped reaction mixture was heated for 5 min at 95°C and centrifuged for 10 min at 11,300 *g*. Twenty microliters of the supernatant was injected onto an Adsorbosphere Nucleotide-Nucleoside RP C18 HPLC column (250 × 4.6 mm; Alltech) equipped with the same type guard column (7.5 × 4.6 mm; Alltech/Grade). As mobile phase, 0.15 *M* NaH_2PO_4 and 40% acetonitrile was used. A relatively rapid linear gradient from 0% to 35% acetonitrile, for 10 min at 1 mL · min^{-1}, was applied to separate GTP, c-di-GMP, and pGpG, with which we could efficiently process the high number of samples produced. Known amounts of all three molecules were used for standardization.

Given the high sensitivity of *Av*GReg to product inhibition, low substrate concentrations were used. When the substrate concentration [S] << K_m, then [S] is almost negligible and the Michaelis–Menten's equation becomes:

$$v_i = \frac{V_{max}[S]}{K_m}.$$

Given that $V_{max} = k_{cat}[E]_0$, in our experimental conditions, the enzyme specificity constant (k_{cat}/K_m) can be calculated from the Michaelis–Menten plots.

Crystallization, structure determination, and refinement

Crystallization of *Av*GReg-Gb and *Bpe*GReg-Gb* was achieved using the sitting drop vapor diffusion method. *Av*GReg-Gb crystals were obtained by equilibrating at 4°C the protein solution (30 mg · mL^{-1}) against 33% PEG 6000 and 10 m*M* Na-citrate. The crystals diffracted up to 2.83 Å resolution, using synchrotron radiation (XRD1 beamline; Elettra-Sincrotrone Trieste S.C.p.A, Trieste, Italy). They belong to the monoclinic $P2_1$ space group with two *Av*GReg-Gb molecules per asymmetric unit (estimated solvent content 33%) (Table 4).

*Bpe*GReg-Gb* crystals grew at 4°C by using two different ionic and pH conditions: 1.6 *M* magnesium sulfate and 0.1 *M* MES, pH 6.5 (condition 1: *Bpe*GReg-Gb*) or 0.8–1 *M* ammonium sulfate and 0.1 *M* Tris-HCl, pH 6.0–9.0 (condition 2: *Bpe*GReg-Gb*-2). The crystals grown under conditions 1 and 2 diffracted up to 3.20 Å and 1.55 Å resolution, respectively, using synchrotron radiation (at SOLEIL and ESRF facilities, France). Both crystal forms belong to the *C*2 space group, but with different cell parameters, and contain two protein molecules in the asymmetric unit (estimated solvent content 48.25% for *Bpe*GReg-Gb* and 34.69% for *Bpe*GReg-Gb*-2) (Table 4). MOSFLM (31), SCALA (18), and the CCP4 suite programs (71) were used for reducing, scaling, and analyzing all the collected data.

The *Bpe*GReg-Gb*-2 structure was solved with a combination of single wavelength anomalous dispersion based on the heme-Fe atom anomalous signal and molecular replacement. Few regions of the structure were built based on the SAD data. This partial model was used to determine the remaining phases with Phaser molecular replacement program (35). The molecular model was checked manually with COOT (17) and refined with REFMAC5 (37, 38) to the maximum resolution (Table 4). The *Bpe*GReg-Gb*-2 refined structure was used as starting model (as a monomer) to solve the *Bpe*GReg-Gb* and the *Av*GReg-Gb dimeric structures with Phaser (35).

The resulting structures were remodeled by using COOT (17) and refined with REFMAC5 (37, 38) (Table 4). Their stereo chemical quality was assessed with MolProbity (9), and the quaternary assemblies were identified with PISA (30). Finally, the atomic coordinates and the structure factors have been deposited in the Protein Data Bank with entry codes 4UII (*Av*GReg-Gb), 6I2Z (*Bpe*GReg-Gb*), and 4UIQ (*Bpe*GReg-Gb*-2).

Acknowledgments

The authors thank Miroslaw Tarnawski and Thomas Barends for making the *Ec*DosC model (full-length) available.

Author Disclosure Statement

No competing financial interests exist.

Funding Information

This work was supported by the Fund of Scientific Research–Flanders (FWO) (Grant number G.0247.09N), the University of Antwerp through the GOA biofilm project 25624 (GOA BOF UA 2011–2014) and the GOA-BOF project 28312. F.G. is a PhD fellow of the Fund of Scientific Research–Flanders (FWO). A.D.S. was funded by a PhD

grant of the Innovation by Science and Technology (121339; IWT, Belgium).

Supplementary Material

Supplementary Figure S1
Supplementary Figure S2
Supplementary Figure S3
Supplementary Figure S4

References

1. Antonini E, and Brunori M. *Hemoglobin and Myoglobin in Their Reactions with Ligands*. Amsterdam, The Netherlands: North-Holland Publishing Company, 1971.
2. Aono S, Kato T, Matsuki M, Nakajima H, Ohta T, Uchida T, and Kitagawa T. Resonance Raman and ligand binding studies of the oxygen-sensing signal transducer protein HemAT from *Bacillus subtilis*. *J Biol Chem* 277: 13528–13538, 2002.
3. Bart MJ, van Gent M, van der Heide HG, Boekhorst J, Hermans P, Parkhill J, and Mooi FR. Comparative genomics of prevaccination and modern *Bordetella pertussis* strains. *BMC Genomics* 11: 627, 2010.
4. Bart MJ, Zeddeman A, van der Heide HG, Heuvelman K, van Gent M, and Mooi FR. Complete genome sequences of *Bordetella pertussis* isolates B1917 and B1920, representing two predominant global lineages. *Genome Announc* 2: pii:e01301–e01314, 2014.
5. Brunori M, and Schuster TM. Kinetic studies of ligand binding to hemoglobin and its isolated subunits by the temperature jump relaxation method. *J Biol Chem* 244: 4046–4053, 1969.
6. Burns JL, Deer DD, and Weinert EE. Oligomeric state affects oxygen dissociation and diguanylate cyclase activity of globin coupled sensors. *Mol Biosyst* 10: 2823–2826, 2014.
7. Burns JL, Rivera S, Deer DD, Joynt SC, Dvorak D, and Weinert EE. Oxygen and bis(3′,5′)-cyclic dimeric guanosine monophosphate binding control oligomerization state equilibria of diguanylate cyclase-containing globin coupled sensors. *Biochemistry* 55: 6642–6651, 2016.
8. Centeno JA. Evidence of dithionite contribution to the low-frequency resonance Raman spectrum of reduced and mixed-valence cytochrome c oxidase. *Arch Biochem Biophys* 292: 624–628, 1992.
9. Chen VB, Arendall WB, III, Headd JJ, Keedy DA, Immormino RM, Kapral GJ, Murray LW, Richardson JS, and Richardson DC. MolProbity: all-atom structure validation for macromolecular crystallography. *Acta Crystallogr D Biol Crystallogr* 66: 12–21, 2010.
10. Conover MS, Sloan GP, Love CF, Sukumar N, and Deora R. The Bps polysaccharide of *Bordetella pertussis* promotes colonization and biofilm formation in the nose by functioning as an adhesin. *Mol Microbiol* 77: 1439–1455, 2010.
11. Das TK, Couture M, Ouellet Y, Guertin M, and Rousseau DL. Simultaneous observation of the O—O and Fe—O_2 stretching modes in oxyhemoglobins. *Proc Natl Acad Sci U S A* 98: 479–484, 2001.
12. Das TK, Friedman JM, Kloek AP, Goldberg DE, and Rousseau DL. Origin of the anomalous Fe-CO stretching mode in the CO complex of *Ascaris* hemoglobin. *Biochemistry* 39: 837–842, 2000.
13. Deinum G, Stone JR, Babcock GT, and Marletta MA. Binding of nitric oxide and carbon monoxide to soluble guanylate cyclase as observed with Resonance Raman spectroscopy. *Biochemistry* 35: 1540–1547, 1996.
14. Dewilde S, Kiger L, Burmester T, Hankeln T, Baudin-Creuza V, Aerts T, Marden MC, Caubergs R, and Moens L. Biochemical characterization and ligand binding properties of neuroglobin, a novel member of the globin family. *J Biol Chem* 276: 38949–38955, 2001.
15. Dewilde S, Mees K, Kiger L, Lechauve C, Marden MC, Pesce A, Bolognesi M, and Moens L. Expression, purification, and crystallization of neuro- and cytoglobin. *Methods Enzymol* 436: 341–357, 2008.
16. Dufour D, Leung V, and Lévesque CM. Bacterial biofilm: structure, function and antimicrobial resistence. *Endod Top* 22: 2–16, 2012.
17. Emsley P, Lohkamp B, Scott WG, and Cowtan K. Features and development of Coot. *Acta Crystallogr D Biol Crystallogr* 66: 486–501, 2010.
18. Evans P. Scaling and assessment of data quality. *Acta Crystallogr D Biol Crystallogr* 62: 72–82, 2006.
19. Freitas TA, Hou S, and Alam M. The diversity of globin-coupled sensors. *FEBS Lett* 552: 99–104, 2003.
20. Germani F, Moens L, and Dewilde S. Haem-based sensors: a still growing old superfamily. *Adv Microb Physiol* 63: 1–47, 2013.
21. Gibson QH, Olson JS, McKinnie RE, and Rohlfs RJ. A kinetic description of ligand binding to *Sperm whale* myoglobin. *J Biol Chem* 261: 10228–10239, 1986.
22. Gilles-Gonzalez MA, Gonzalez G, Perutz MF, Kiger L, Marden MC, and Poyart C. Heme-based sensors, exemplified by the kinase FixL, are a new class of heme protein with distinctive ligand binding and autoxidation. *Biochemistry* 33: 8067–8073, 1994.
23. Guttenplan SB, and Kearns DB. Regulation of flagellar motility during biofilm formation. *FEMS Microbiol Rev* 37: 849–871, 2013.
24. Hirota S, Ogura T, Appelman EH, Shinzawaitoh K, Yoshikawa S, and Kitagawa T. Observation of a new oxygen-isotope-sensitive Raman band for oxyhemoproteins and its implication in heme pocket structures. *J Am Chem Soc* 116: 10564–10570, 1994.
25. Hu SZ, Smith K, and Spiro TG. Assignment of protoheme resonance Raman spectrum by heme labeling in myoglobin. *J Am Chem Soc* 118: 12638–12646, 1996.
26. Jenal U, Reinders A, and Lori C. Cyclic di-GMP: second messenger extraordinaire. *Nat Rev Microbiol* 15:271–284, 2017.
27. Kerr EA, Yu NT, Bartnicki DE, and Mizukami H. Resonance Raman studies of CO and O_2 binding to elephant myoglobin (distal His(E7)—Gln). *J Biol Chem* 260: 8360–8365, 1985.
28. Kitanishi K, Kobayashi K, Kawamura Y, Ishigami I, Ogura T, Nakajima K, Igarashi J, Tanaka A, and Shimizu T. Important roles of Tyr43 at the putative heme distal side in the oxygen recognition and stability of the Fe(II)-O_2 complex of YddV, a globin-coupled heme-based oxygen sensor diguanylate cyclase. *Biochemistry* 49: 10381–10393, 2010.
29. Kitanishi K, Kobayashi K, Uchida T, Ishimori K, Igarashi J, and Shimizu T. Identification and functional and spectral characterization of a globin-coupled histidine kinase from *Anaeromyxobacte*r sp. Fw109-5. *J Biol Chem* 286: 35522–35534, 2011.
30. Krissinel E, and Henrick K. Inference of macromolecular assemblies from crystalline state. *J Mol Biol* 372: 774–797, 2007.

31. Leslie AG. The integration of macromolecular diffraction data. *Acta Crystallogr D Biol Crystallogr* 62: 48–57, 2006.
32. Martinez LC, and Vadyvaloo V. Mechanisms of post-transcriptional gene regulation in bacterial biofilms. *Front Cell Infect Microbiol* 4: 38, 2014.
33. Martinkova M, Kitanishi K, and Shimizu T. Heme-based globin-coupled oxygen sensors: linking oxygen binding to functional regulation of diguanylate cyclase, histidine kinase, and methyl-accepting chemotaxis. *J Biol Chem* 288: 27702–27711, 2013.
34. Maunders E, and Welch M. Matrix exopolysaccharides; the sticky side of biofilm formation. *FEMS Microbiol Lett* 363: fnx120, 2017.
35. McCoy AJ, Grosse-Kunstleve RW, Adams PD, Winn MD, Storoni LC, and Read RJ. Phaser crystallographic software. *J Appl Crystallogr* 40: 658–674, 2007.
36. Mishra M, Parise G, Jackson KD, Wozniak DJ, and Deora R. The BvgAS signal transduction system regulates biofilm development in *Bordetella*. *J Bacteriol* 187: 1474–1484, 2005.
37. Murshudov GN, Vagin AA, and Dodson EJ. Refinement of macromolecular structures by the maximum-likelihood method. *Acta Crystallogr D Biol Crystallogr* 53: 240–255, 1997.
38. Murshudov GN, Vagin AA, Lebedev A, Wilson KS, and Dodson EJ. Efficient anisotropic refinement of macromolecular structures using FFT. *Acta Crystallogr D Biol Crystallogr* 55: 247–255, 1999.
39. Nagai K, Kitagawa T, and Morimoto H. Quaternary structures and low frequency molecular vibrations of haems of deoxy and oxyhaemoglobin studied by resonance Raman scattering. *J Mol Biol* 136: 271–289, 1980.
40. Nardini M, Pesce A, Thijs L, Saito JA, Dewilde S, Alam M, Ascenzi P, Coletta M, Ciaccio C, Moens L, and Bolognesi M. Archaeal protoglobin structure indicates new ligand diffusion paths and modulation of haem-reactivity. *EMBO Rep* 9: 157–163, 2008.
41. Olson JS. Stopped-flow, rapid mixing measurements of ligand binding to hemoglobin and red cells. *Methods Enzymol* 76: 631–651, 1981.
42. Olson JS, Foley EW, Maillet DH, and Paster EV. Measurement of rate constants for reactions of O_2, CO and NO with hemoglobin. In: *Hemoglobin Disorders, Methods in Molecular Biology*, edited by Nagel RL. Totowa NJ: Humana Press, Inc., 2003, 82, 65–91.
43. Othman S, Richaud P, Vermeglio A, and Desbois A. Evidence for a proximal histidine interaction in the structure of cytochromes c in solution: a resonance Raman study. *Biochemistry* 35: 9224–9234, 1996.
44. Pesce A, Nardini M, Dewilde S, Ascenzi P, Burmester T, Hankeln T, Moens L, and Bolognesi M. Human neuroglobin: crystals and preliminary X-ray diffraction analysis. *Acta Crystallogr D Biol Crystallogr* 58: 1848–1850, 2002.
45. Pesce A, Thijs L, Nardini M, Desmet F, Sisinni L, Gourlay L, Bolli A, Coletta M, Van DS, Wan X, Alam M, Ascenzi P, Moens L, Bolognesi M, and Dewilde S. HisE11 and HisF8 provide bis-histidyl heme hexa-coordination in the globin domain of *Geobacter sulfurreducens* globin-coupled sensor. *J Mol Biol* 386: 246–260, 2009.
46. Pesce A, Tilleman L, Dewilde S, Ascenzi P, Coletta M, Ciaccio C, Bruno S, Moens L, Bolognesi M, and Nardini M. Structural heterogeneity and ligand gating in ferric *Methanosarcina acetivorans* protoglobin mutants. *IUBMB Life* 63: 287–294, 2011.
47. Pesce A, Tilleman L, Donne J, Aste E, Ascenzi P, Ciaccio C, Coletta M, Moens L, Viappiani C, Dewilde S, Bolognesi M, and Nardini M. Structure and haem-distal site plasticity in *Methanosarcina acetivorans* protoglobin. *PLoS One* 8: e66144, 2013.
48. Poole RK, and Hill S. Respiratory protection of nitrogenase activity in *Azotobacter vinelandii*—roles of the terminal oxidases. *Biosci Rep* 17: 303–317, 1997.
49. Purcell EB, and Tamayo R. Cyclic diguanylate signaling in Gram-positive bacteria. *FEMS Microbiol Rev* 40: 753–773, 2016.
50. Rivera S, Burns JL, Vansuch GE, Chica B, and Weinert EE. Globin domain interactions control heme pocket conformation and oligomerization of globin coupled sensors. *J Inorg Biochem* 164: 70–76, 2016.
51. Rivera S, Young PG, Hoffer ED, Vansuch GE, Metzler CL, Dunham CM, and Weinert EE. Structural insights into oxygen-dependent signal transduction within globin coupled sensors. *Inorg Chem* 57: 14386–14395, 2018.
52. Römling U, and Galperin MY. Discovery of the second messenger Cyclic di-GMP. *Methods Mol Biol* 1657: 1–8, 2017.
53. Ryan RP. Cyclic di-GMP signalling and the regulation of bacterial virulence. *Microbiology* 159: 1286–1297, 2013.
54. Ryjenkov DA, Tarutina M, Moskvin OV, and Gomelsky M. Cyclic diguanylate is a ubiquitous signaling molecule in bacteria: insights into biochemistry of the GGDEF protein domain. *J Bacteriol* 187: 1792–1798, 2005.
55. Setubal JC, Dos SP, Goldman BS, Ertesvag H, Espin G, Rubio LM, Valla S, Almeida NF, Balasubramanian D, Cromes L, Curatti L, Du Z, Godsy E, Goodner B, Hellner-Burris K, Hernandez JA, Houmiel K, Imperial J, Kennedy C, Larson TJ, Latreille P, Ligon LS, Lu J, Maerk M, Miller NM, Norton S, O'Carroll IP, Paulsen I, Raulfs EC, Roemer R, Rosser J, Segura D, Slater S, Stricklin SL, Studholme DJ, Sun J, Viana CJ, Wallin E, Wang B, Wheeler C, Zhu H, Dean DR, Dixon R, and Wood D. Genome sequence of *Azotobacter vinelandii*, an obligate aerobe specialized to support diverse anaerobic metabolic processes. *J Bacteriol* 191: 4534–4545, 2009.
56. Shimizu T, Huang D, Yan F, Stranava M, Bartosova M, Fojtikova V, and Martinkova M. Gaseous O_2, NO, and CO in signal transduction: structure and function relationships of heme-based gas sensors and heme-redox sensors. *Chem Rev* 115: 6491–6533, 2015.
57. Sondermann H, Shikuma NJ, and Yildiz FH. You've come a long way: c-di-GMP signaling. *Curr Opin Microbiol* 15: 140–146, 2012.
58. Song S, Boffi A, Chiancone E, and Rousseau DL. Protein-heme interactions in hemoglobin from the mollusc *Scapharca inaequivalvis*: evidence from resonance Raman scattering. *Biochemistry* 32: 6330–6336, 1993.
59. Spiro TG, and Li XY. Resonance Raman spectroscopy of metalloporphyrins. In: Spiro TG (ed). *Biological applications of Raman spectroscopy*, Vol. 3. New York: John Wiley & Sons, 1988, pp. 1–37.
60. Takahashi S, Ishikawa, Takeuchi N, Ikeda-Saito M, Yoshida Y, and Rousseau DL. Oxygen-bound heme-heme oxygenase complex: evidence for a highly bent structure of the coordinated oxygen. *J Am Chem Soc* 117: 6002–6006, 1995.
61. Takahashi S, Wang J, Rousseau DL, Ishikawa K, Yoshida T, Takeuchi N, and Ikeda-Saito M. Heme-heme oxygenase

complex: structure and properties of the catalytic site from resonance Raman scattering. *Biochemistry* 33: 5531–5538, 1994.
62. Tamura K, Tanaka Y, Oue S, Tsukamoto K, Nomura M, Tsuchiya T, Adachi S, Takahashi S, Iizuka T, and Shiro Y. Nature of endogenous ligand binding to heme iron in oxygen sensor FixL. *J Am Chem Soc* 118: 9434–9435, 1996.
63. Tarnawski M, Barends TR, and Schlichting I. Structural analysis of an oxygen-regulated diguanylate cyclase. *Acta Crystallogr D Biol Crystallogr* 71: 2158–2177, 2015.
64. Thijs L, Vinck E, Bolli A, Trandafir F, Wan X, Hoogewijs D, Coletta M, Fago A, Weber RE, Van Doorslaer S, Ascenzi P, Alam M, Moens L, and Dewilde S. Characterization of a globin-coupled oxygen sensor with a gene-regulating function. *J Biol Chem* 282: 37325–37340, 2007.
65. Tomita T, Ogura T, Tsuyama S, Imai Y, and Kitagawa T. Effects of GTP on bound nitric oxide of soluble guanylate cyclase probed by resonance Raman spectroscopy. *Biochemistry* 36: 10155–10160, 1997.
66. Tsai AL, Berka V, Martin E, and Olson JS. A ''sliding scale rule'' for selectivity among NO, CO and O_2 by heme protein sensors. *Biochemistry* 51: 172–186, 2012.
67. Uchida T, Ishikawa H, Takahashi S, Ishimori K, Morishima I, Ohkubo K, Nakajima H, and Aono S. Heme environmental structure of CooA is modulated by the target DNA binding. Evidence from resonance Raman spectroscopy and CO rebinding kinetics. *J Biol Chem* 273: 19988–19992, 1998.
68. Uchida T, and Kitagawa T. Mechanism for transduction of the ligand-binding signal in heme-based gas sensory proteins revealed by resonance Raman spectroscopy. *Acc Chem Res* 38: 662–670, 2005.
69. Vinogradov SN, and Moens L. Diversity of globin function: enzymatic, transport, storage, and sensing. *J Biol Chem* 283: 8773–8777, 2008.
70. Wan X, Tuckerman JR, Saito JA, Freitas TA, Newhouse JS, Denery JR, Galperin MY, Gonzalez G, Gilles-Gonzalez MA, and Alam M. Globins synthesize the second messenger bis-(3′-5′)-cyclic diguanosine monophosphate in bacteria. *J Mol Biol* 388: 262–270, 2009.
71. Winn MD, Ballard CC, Cowtan KD, Dodson EJ, Emsley P, Evans PR, Keegan RM, Krissinel EB, Leslie AG, McCoy A, McNicholas SJ, Murshudov GN, Pannu NS, Potterton EA, Powell HR, Read RJ, Vagin A, and Wilson KS. Overview of the CCP4 suite and current developments. *Acta Crystallogr D Biol Crystallogr* 67: 235–242, 2011.
72. Yang J, Yan R, Roy A, Xu D, Poisson J, Zhang Y. The I-TASSER Suite: protein structure and function prediction. *Nat Methods* 12: 7–8, 2015.
73. Yeh SH. Pertussis: persistent pathogen, imperfect vaccines. *Expert Rev Vaccines* 2: 113–127, 2003.
74. Yeh SR, Couture M, Ouellet Y, Guertin M, and Rousseau DL. A cooperative oxygen binding hemoglobin from *Mycobacterium tuberculosis*. Stabilization of heme ligands by a distal tyrosine residue. *J Biol Chem* 275: 1679–1684, 2000.
75. Zhang W, and Phillips GN, Jr. Structure of the oxygen sensor in *Bacillus subtilis*: signal transduction of chemotaxis by control of symmetry. *Structure* 11: 1097–1110, 2003.

Address correspondence to:
Dr. Alessandra Pesce
Department of Physics
University of Genova
Via Dodecaneso 33
I-16146 Genova
Italy

E-mail: pesce@fisica.unige.it

Dr. Sylvia Dewilde
Department of Biomedical Sciences
University of Antwerp
Universiteitsplein 1
B-2610 Wilrijk
Belgium

E-mail: sylvia.dewilde@uantwerpen.be

Date of first submission to ARS Central, November 8, 2018; date of final revised submission, September 12, 2019; date of acceptance, September 21, 2019.

Abbreviations Used

*Af*GcHK = globin-coupled histidine kinase from *Anaeromyxobacter sp.* Fw109-5
*Av*GReg = globin-coupled sensor from *Azotobacter vinelandii*
*Av*GReg-Gb = *Av*GReg globin domain
*Av*GRegYB10F = *Av*GReg with Tyr(44) mutated to Phe
*Bpe*GReg = globin-coupled sensor from *Bordetella pertussis*
*Bpe*GReg* = *Bpe*GReg with cysteines (Cys16, 45, 114, 154) mutated to serines
*Bpe*GReg-Gb = *Bpe*GReg globin domain
*Bpe*GReg-Gb* = *Bpe*GRegGb with cysteines (Cys16, 45, 114, 154) mutated to serines
*Bs*HemAT = *Bacillus subtilis* heme-based aerotaxis transducer
c-di-GMP = cyclic-di-(3′,5′)-GMP
CO = carbon monoxide
DGC = diguanylate cyclase
*Ec*DosC = *Escherichia coli* globin-coupled sensor with DGC activity
*Ec*DosC-heme = isolated globin domain of the *E. coli* globin-coupled sensor
FTIR = Fourier transform infrared
GCS = globin-coupled sensor
*Gs*GCS^{162} = sensor domain from the *Geobacter sulfurreducens* globin-coupled sensor
PCR = polymerase chain reaction
PDE = phosphodiesterase
rmsd = root mean squared deviation
RR = resonance Raman
*Sw*Mb = sperm whale myoglobin
UV/Vis = ultraviolet/visible